עבודת גמר (תזה) לתואר
דוקטור לפילוסופיה

מוגשת למועצה המדעית של
מכון ויצמן למדע
רחובות, ישראל

Thesis for the degree
Doctor of Philosophy

Submitted to the Scientific Council of the
Weizmann Institute of Science
Rehovot, Israel

במתכונת "רגילה"
In a "Regular" Format

מאת
שרה גולדברג

By
Sarah Goldberg

השראה ובדיקה של סדר ארוך-טווח של החומר המערבולתי במוליכי על בעלי T_c גבוה

Inducing and Probing Long-range Order of the Vortex Matter in High-T_c Superconductors

מנחה:
פרופ. אלי זלדוב

Advisor:
Prof. Eli Zeldov

אדר התשס"ט

February 2009

Acknowledgements

אַתָּה חוֹנֵן לְאָדָם דַּעַת, וּמְלַמֵּד לֶאֱנוֹשׁ בִּינָה, חָנֵּנוּ מֵאִתְּךָ דֵּעָה בִּינָה וְהַשְׂכֵּל.
(מתוך תפילת העמידה)

I would like to thank the many people who provided technical, theoretical, and moral support during the past years.

I thank my advisor, Eli Zeldov, for the idea that started the Bragg-MO project, for many clarifying discussions along the way, and for his patience.

I thank Beena Kalisky for being both a fun research partner and a great teacher. Special thanks go to Yuri Myasoedov for helping with sample preparation and to Yehonathan Segev for his time and efforts spent in fabrication of surface holes.

I am thankful to Yadin Goldschmidt and to Michael Opferman for a constructive collaboration that unfortunately ended too soon. Thanks also to Michael Baziljevich for his input, to Michael Golub for theoretical calculations and to Ilan Barboy for suggesting the use of magnetic tapes.

I thank Michael Rappaport for his help in solving various technical problems and Enrico Segre for software solutions. I thank Yehuda Asher, Shlomo Assayag, Solomon Shpiner, Yossi Gal, Ronen Havkin and Lee Levitt for their accommodating attitude and technical support. I thank the many people from the optics labs who generously lent both equipment and advice, among them Dan Oron, Eran Tal, Evgeny Frumker, Nadav Katz and Tzahi Grunzweig.

I thank the members of my thesis committee, Dan Shahar and Ady Stern, for their support.

I thank group members Tal Verdene, Nurit Avraham, Haim Beidenkopf, Ilia Gutman, Amit Finkler and Satya Banerjee for the truly positive atmosphere in the lab.

Finally, I thank my husband Yair for his constant encouragement and support.

1. Abstract

In this work we measured high-T_c superconducting $Bi_2Sr_2CaCu_2O_{8+\delta}$ (BSCCO) samples with periodic surface holes created by a focused ion beam using differential magneto-optics with field modulation. We found that the dynamic irreversibility line of the patterned regions is shifted to higher magnetic fields and temperatures with respect to that of the pristine material. The irreversibility line displays step-like behavior, with weak temperature dependence between matching fields. We discuss why these steps are consistent with a multi-quanta vortex scenario. We also found that in narrow regions of the H-T phase diagram corresponding to integer matching fields, the compressibility of the vortex matter is reduced considerably. Measurements in the vicinity of these matching fields using magneto-optics combined with the shaking technique indicated that the regions of reduced compressibility are equilibrium Mott insulator phases of the vortex matter in the presence of periodic surface holes. Surprisingly, a first-order melting transition occurs even within these phases of reduced-compressibility. We discuss this apparent discrepancy.

In a related project, we constructed the novel Bragg magneto-optical microscope that images the diffraction pattern of samples with periodic magnetic induction. We demonstrated that this microscope is capable of measuring diffraction from periodic magnetic recordings with spatial spacing and magnetic induction amplitude nearing those of the vortex lattice within a type II superconducting sample. We also demonstrated that the zeroth order of the diffraction pattern can be used as a probe of the average magnetic induction. We showed that with sufficient averaging, the zeroth order can be used to probe signals as low as 0.1 G, the typical magnitude of both the magnetization step at the first-order melting transition in BSCCO and the dip feature at matching fields in BSCCO samples with periodic surface holes.

Contents

2. Introduction

High-temperature superconductors provide a fascinating and convenient model system for the study of thermodynamic phenomena. In the mixed state of these type-II materials, magnetic fields penetrate in the form of vortices, or flux lines, each with a single flux quantum. These vortices are in fact a system of interacting particles, whose properties depend on adjustable experimental parameters. Vortex density may be changed by varying the applied field. The degree of thermal fluctuations of the vortices may be changed by varying the temperature. Various forms of introduced disorder, such as point defects introduced by electron irradiation and columnar defects introduced by heavy-ion irradiation, also affect the properties of the vortex system. The phase diagram of the vortex matter in high-temperature superconductors is complex, exhibiting a variety of thermodynamic phases and phase transitions, many of which are not fully understood.

Detecting such phase transitions requires experimental probes that are sensitive to changes in the physical properties of the vortex matter. Magnetic measurements provide a probe of the vortex density. Differential magnetic measurements are particularly useful in locating jumps in vortex density, which indicate first-order transitions of the vortex matter. These measurements also provide information regarding the compressibility of the vortex matter. Another experimental probe of the vortex matter is the diffraction pattern of the magnetic induction. The magnetic induction varies spatially, with local maxima wherever vortices are located. The location of the first-order diffraction peaks provides information regarding the average spacing of the vortices and the orientation of the quasi-ordered vortex matter. The structure of the first-order peaks provides information regarding the degree of long-range order of the vortex matter. The intensity of the peaks relative to the zero-order intensity provides information regarding the amplitude of

the modulation in magnetic induction due to the presence of the vortices.

This research addresses questions related to the degree of long-range order in the vortex matter of the high-temperature superconductors. Two different projects are presented. In the first project, we study the effects of ordered surface holes on the phase diagram of $Bi_2Sr_2CaCu_2O_{8+\delta}$ crystals, using differential magneto-optical measurements. The in-plane shaking technique was applied to hasten equilibration of the vortex system, thus enabling the observation of equilibrium properties. We find that surface holes induce reduced equilibrium compressibility of the vortex matter at so-called matching-fields, namely fields at which the hole and vortex densities are commensurate. These reduced-compressibility phases indicate that the vortex matter is in a commensurate state with a high degree of long-range order at matching fields. Despite the reduced compressibility of the "tips" of the vortices at the surface, the "tails" of the vortices located in the bulk beneath the surface holes undergo a first-order melting transition.

In the second project, we constructed the novel Bragg magneto-optical microscope, in order to measure the diffraction image of a superconducting sample with periodic magnetic induction. We demonstrated that this microscope is capable of measuring diffraction patterns at room temperature from samples with periodic magnetic induction, where both the periodicity and the modulation amplitude of the periodic magnetic induction approach the scales relevant to vortex matter. The ultimate goal of this microscope is to provide quantitative information regarding the density, orientation, and long-range order of the vortex matter at different points in the phase diagram.

This thesis is organized as follows. Chapter 3 provides a basic overview of superconductivity and vortex matter. The various measurement techniques used in this research are described in Chapter 4. Both the differential and Bragg magneto-optical setups are described in Chapter 5. Experimental results are presented and discussed in Chapter 6. Chapter 7 provides a summary of our main findings. A list of publications appears in Chapter 8.

3. Scientific Background

3.1 Basic Properties of Superconductors

The first basic property of superconductors, "perfect conductivity", was discovered by H. K. Onnes in 1911 [1]. He found that various materials exhibited zero resistivity below a material-dependent critical temperature T_c. The technological importance of this discovery was immediately recognized: current could be driven through a superconducting material without measurable losses. In 1913, Onnes further discovered that this zero resistivity state existed only for current densities below some critical current density $J_c(T)$, and for applied magnetic fields below a critical field $H_c(T)$.

The second basic property, "perfect diamagnetism" or the "Meissner effect", was discovered by W. Meissner and R. Oschenfeld in 1933 [2]. They found that bulk superconducting materials behave as perfect diamagnets below a temperature-dependent critical field $H_c(T)$. For external magnetic fields below $H_c(T)$, the magnetic induction of the bulk is zero for any value of the external magnetic field, and the superconductor is in the Meissner phase. Above $H_c(T)$, the superconductor is in its normal phase.

Both perfect conductivity and the lack of dissipation in superconducting wires in the presence of persistent currents [3] led to the concept of a finite energy gap between the superconducting ground state and the excitations of the system. Evidence of such a gap was provided by specific heat [4] and microwave transmission [5] measurements, with the measured energy gap on the order of $K_B T_c$. It was later understood [6, 7, 8, 9] and demonstrated [10, 11] that gapless superconductivity exists, for instance in the presence of magnetic impurities. Also, the energy gap structures of certain superconductors exhibit gapless nodes [12]. However, the energy gap was and remains essential to the theoretical understanding of superconductivity.

3.2 Theory of Superconductivity

3.2.1 London Theory

A phenomenological description for the two basic properties of superconductors was proposed by F. and H. London in 1935 [13]. This description was given as a set of equations, called the "London equations", for the local electric and magnetic fields **E** and **B**:

$$\begin{aligned} \mathbf{E} &= \frac{\partial}{\partial t}\left(\frac{m}{n_s e^2}\mathbf{J}_s\right) \\ \mathbf{B} &= -c\nabla \times \left(\frac{m}{n_s e^2}\mathbf{J}_s\right), \end{aligned} \tag{3.1}$$

where $\mathbf{J}_s$ is the superconducting current, understood to be carried by superconducting electrons with density n_s. The first London equation describes perfect conductivity, since **E** accelerates the superconducting electrons and there is no decelerating (Drude) term corresponding to scattering. The second London equation, combined with the Maxwell equation $\nabla \times \mathbf{B} = 4\pi\mathbf{J}_s/c$, gives

$$\nabla^2\mathbf{B} = \frac{\mathbf{B}}{\lambda_L^2}, \tag{3.2}$$

where

$$\lambda_L = \sqrt{\frac{mc^2}{4\pi n_s e^2}}. \tag{3.3}$$

Equation 3.2 describes the Meissner effect: an external magnetic field is exponentially screened from the interior of a superconductor, decaying over a typical distance λ_L from the surface, called the penetration depth.

3.2.2 BCS Theory

A microscopic description of superconductivity was given in 1957 by J. Bardeen, L. N. Cooper and J. R. Schrieffer (BCS) [14]. The BCS theory explained that the superconducting electronic ground state was in fact a condensate of electron pairs, termed "Cooper pairs", bound together by phonon-mediated interaction. This ground state was shown to be protected against excitations by an energy gap $\Delta(T)$, that is finite below T_c and drops to zero as T_c is approached from below. The calculated value of $\Delta(T)$ was shown to be on the order of $K_B T_c$, in agreement with experiments. The energy gap explains the perfect

conductivity exhibited by superconductors. As long as the thermal energy of the ionic lattice is lower than Δ, the Cooper pairs moving in the lattice cannot be scattered by the lattice, and will therefore exhibit dissipationless flow. The finite energy difference between the superconducting ground state and the normal state defines the thermodynamic condensation energy $H_c(T)^2/8\pi$. For applied fields below the critical field $H_c(T)$, the energy invested in screening the field is lower than the condensation energy, resulting in the Meissner state. When the applied field exceeds $H_c(T)$, the normal state is energetically preferred. The correct scale for the critical current J_c can be deduced from equating the kinetic energy density of the electrons $n_s m v_c^2/2 = 2\pi\lambda_L^2 J_c^2/c^2$ to the condensation energy $H_c^2/8\pi$, resulting in $J_c = cH_c/4\pi\lambda_L$.

BCS theory also introduced the length-scale ξ, known as the coherence length, which is a measure of the spatial size of a Cooper pair. According to BCS theory, superconducting electrons come mainly from a narrow energy window of $K_B T_c$ around the Fermi energy, resulting in a momentum spread of $\Delta p \sim K_B T_c/v_F$, or a spatial spread of $\xi \sim \hbar/\Delta p = \hbar v_F/K_B T_c$.

3.2.3 Ginzburg-Landau Theory

In 1950, V. L. Ginzburg and L. D. Landau (GL) developed what was then considered a phenomenological theory for superconductivity [15], that allowed for spatial variations of the superfluid electron density n_s. GL theory was shown to be a limiting case of the BCS theory by L. P. Gor'kov in 1959 [16], for temperatures not far from T_c and spatial variations of the vector potential $\mathbf{A}$ and n_s that are not too rapid. It enables simpler treatment of the macroscopic behavior of superconductors than BCS theory.

GL theory assumes the existence of a complex order parameter $\psi(x)$, that is equal to the superfluid pair density $|\psi(x)|^2 = n_s/2$. It is assumed that ψ is finite in the superconducting state, and zero in the normal state. The free energy density of the system f is written as an expansion in terms of ψ and $\nabla\psi$:

$$f = f_n + \alpha|\psi(x)|^2 + \frac{\beta}{2}|\psi|^4 + \frac{1}{2m^*}|(-i\hbar\nabla - \frac{e^*}{c}\mathbf{A})\psi|^2 + \frac{\mathbf{B}^2}{8\pi}\,, \tag{3.4}$$

where f_n is the energy density of the normal state, and m^* and e^* are the effective mass

and charge (taken as twice the electron mass and charge, due to Cooper pairing).

Minimizing $F = \int d^3r f$ with respect to ψ^* and $\mathbf{A}$ yields the GL equations

$$\alpha\psi + \beta|\psi|^2\psi + \frac{1}{2m^*}(-i\hbar\nabla - \frac{e^*}{c}\mathbf{A})^2\psi = 0 \tag{3.5}$$

$$\frac{c}{4\pi}\nabla \times \mathbf{B} = \frac{-ie^*\hbar}{2m^*}(\psi^*\nabla\psi - \psi\nabla\psi^*) - \frac{e^{*2}}{m^*c}|\psi|^2\mathbf{A}\,. \tag{3.6}$$

These equations have two special solutions. The first is $\psi = 0$ (and $\mathbf{B} = \nabla \times \mathbf{A}$), which describes the normal state. The second is $|\psi|^2 = -\alpha/\beta$ and $\mathbf{A} = 0$, which describes the Meissner state deep within the superconductor, where all external fields are screened. The coefficients α and β can be written in terms of H_c and λ_L, by noting that $f_n - f_s = -\frac{\alpha}{2\beta} = \frac{H_c^2}{8\pi}$ and ${\lambda_L}^2 = \frac{m^*c^2}{4\pi|\psi|^2e^{*2}}$, as [17]

$$\alpha = -\frac{e^{*2}}{m^*c^2}{H_c}^2\lambda_L^2\,, \quad \beta = \frac{4\pi e^{*4}}{m^{*2}c^4}{H_c}^2\lambda_L^4\,. \tag{3.7}$$

From the GL equations, two length-scales arise, corresponding to the length-scales over which spatial variations of ψ and $\mathbf{A}$ occur. The first GL equation, with $\mathbf{A} = 0$ and $\widetilde{\psi} = \sqrt{\beta/|\alpha|}\psi$ dimensionless, can be written as

$$\frac{\hbar^2}{2m^*|\alpha|}\nabla^2\widetilde{\psi} + \widetilde{\psi} - \widetilde{\psi}|\widetilde{\psi}|^2 = 0\,, \tag{3.8}$$

resulting in the definition of the coherence length

$$\xi = \frac{\hbar}{\sqrt{2m^*|\alpha|}}\,. \tag{3.9}$$

The second GL equation can be written as

$$\frac{m^*c^2\beta}{4\pi e^{*2}|\alpha|}\nabla \times (\nabla \times \mathbf{A}) + |\widetilde{\psi}|^2\mathbf{A} + \frac{i\hbar c}{2e^*}(\widetilde{\psi}^*\nabla\widetilde{\psi} - \widetilde{\psi}\nabla\widetilde{\psi}^*)\,, \tag{3.10}$$

resulting in the definition of the penetration depth

$$\lambda = \sqrt{\frac{m^*c^2\beta}{4\pi e^{*2}|\alpha|}}\,, \tag{3.11}$$

which equals the penetration depth λ_L introduced in Eq. 3.3.

As shown in Fig. 3.1, ξ and λ are the scales over which the superconducting density and magnetic flux vary at a normal-superconducting boundary. This means that within the superconductor, there is an energy loss over distance ξ due to loss of condensation, and an energy gain over distance λ due to the reduction in shielding currents. The GL parameter $\kappa = \lambda/\xi$ quantifies the relative magnitude of these two energies.

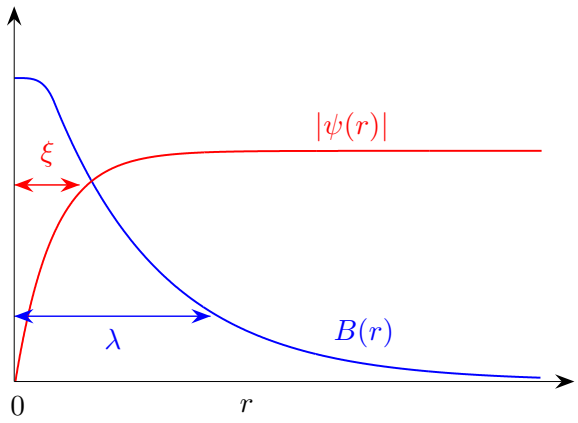

Fig. 3.1: *Magnetic induction $B(r)$ and modulus of order parameter $|\psi(r)|$ as a function of the distance r from a normal-superconducting interface, or from a vortex core.*

3.3 Type I vs. Type II Superconductors

In 1957, A. A. Abrikosov showed that GL theory leads to two different types of superconductors, depending on the value of the GL parameter κ [18]. He found that for type I materials, or materials with $\kappa \leq 1/\sqrt{2}$, there is no penetration of magnetic field into the superconductor below the critical field $H_c(T)$, and homogeneous penetration above $H_c(T)$. For type II materials, namely those with $\kappa > 1/\sqrt{2}$, he predicted that there would exist an additional "mixed state" in which there would be partial penetration of magnetic flux into the material. In this "mixed state", flux penetrates in a way that maximizes the interface between normal and superconducting regions, due to negative normal-superconducting interface energy. Due to the fact that the superconducting wave function must be single-valued, flux is quantized in units of $\phi_0 = hc/2e = 20.67\ \mathrm{G}\mu\mathrm{m}^2$ (with $2e$ due to the double charge of Cooper pairs). The result is penetration of flux in the form of an Abrikosov vortex, namely a topological excitation with a normal core, carrying one quantum of magnetic flux. The core of the vortex behaves like any other normal interface: the magnetic induction decays on a lengthscale of λ from the core, and the order parameter grows on a lengthscale of ξ (see Fig. 3.1).

In type II materials, there is a transition at $H_{c_1}(T)$ from the Meissner phase to the "mixed phase" in which flux penetrates in the form of vortices, and an additional transition

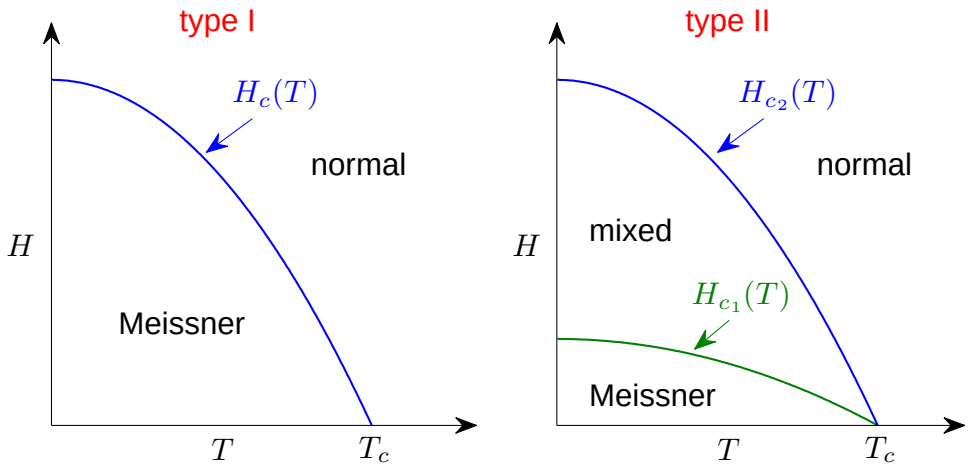

Fig. 3.2: *Schematic $H-T$ phase diagrams of type I and type II superconductors.*

to the normal phase at $H_{c_2}(T)$, where the normal cores of the vortices begin to overlap. The schematic $H-T$ phase diagrams of type I and type II superconductors are shown in Fig. 3.2.

The screening current $\mathbf{j}$ of a single vortex applies a Lorentz force of $F_L = \mathbf{j} \times \phi_0 \mathbf{z}$ on the other vortices, where $\mathbf{z}$ is a unit vector along each vortex, leading to a repulsive interaction between vortices. Minimization of the free energy of a type II superconductor in the mixed state, in the absence of thermal effects and disorder, yields a triangular lattice of vortices, with lattice spacing

$$a_0 = \left(\frac{4}{3}\right)^{1/4} \left(\frac{\phi_0}{B}\right)^{1/2}. \tag{3.12}$$

The vortex lattice of type II superconductors has been observed directly using various experimental methods, including Bitter decoration [19], scanning-tunneling microscopy [20], Hall-probe microscopy [21], Lorentz microscopy [22], and magneto-optics [23].

In the mixed phase, the perfect conductivity of the superconducting material is destroyed by any motion of vortices and its associated energy dissipation. A driving current J applies a force of $F_L = \mathbf{J} \times \phi_0 \mathbf{z}$, which results in vortex motion in the direction transverse to the driving current, and therefore to finite resistivity. In pristine materials, inhomogeneities act as pinning centers and restrain vortex motion for sufficiently low current densities, so that perfect conductivity is still possible. Vortex motion may be suppressed

at even higher current densities by artificially-introduced pinning centers, such as columnar defects resulting from heavy-ion irradiation, or holes created using various milling techniques.

3.4 Vortex Matter in High-T_c Superconductors

High-T_c superconductors are a class of type II superconductors, the first of which was discovered by J. G. Bednorz and K. A. Müller in 1986 [24]. Their discovery of a new superconducting structure, with layers of copper oxide planes separated by metallic or insulating materials, led to the discovery of additional superconductors, including $YBa_2Cu_3O_7$ (YBCO) and $Bi_2Sr_2CaCu_2O_8$ (BSCCO). The critical temperatures of some high-T_c superconductors exceed 130 K. Their critical temperatures may be significantly higher than the liquification temperature of nitrogen, rendering them extremely important from a practical point of view. High-T_c superconductors do not display the usual "isotope effect", indicating that the pairing of electrons may not be phonon-mediated. The microscopic mechanism of superconductivity in the high-T_c materials is not well understood yet.

The layered structure of the high-T_c materials leads to strong anisotropy between the directions parallel and perpendicular to the copper-oxide planes, referred to as the a-b and c axes, respectively. Cooper pairs reside in the copper-oxide planes, while the material between the planes acts as a barrier for inter-plane tunneling of Cooper pairs. This leads to a layered structure of the vortices. When a magnetic field is applied along the c axis, flux penetrates the copper-oxide planes. Within the copper-oxide planes, vortices can be described as two-dimensional "pancake" vortices. Any a-b component of a magnetic field penetrates in the form of Josephson vortices, which reside between the copper-oxide layers and connect pancake vortices in adjacent planes. The interaction between pancake vortices in the same plane is repulsive, while pancake vortices in adjacent layers are weakly coupled by magnetic and Josephson interactions. This results in three-dimensional vortices that are in fact stacks of two-dimensional pancakes, rather weakly coupled along the c axis. These stacked vortices are repulsive, leading to a pancake vortex lattice configuration.

3.4.1 Pristine Samples

Finite temperatures cause vortices to fluctuate about their equilibrium positions. This is particularly relevant in high-T_c materials, due both to their high critical temperatures and to their layered structure, which results in weaker coupling of pancake vortices along the c axis. When the energy of thermal fluctuations is comparable to the elastic energy barriers that keep the vortices near their equilibrium positions in the lattice, the ordered vortex lattice undergoes a melting transition into a disordered vortex liquid [25]. Theoretically, this transition was predicted to be a first-order transition in clean systems [26]. The existence of a first-order solid-liquid transition was established by various experimental techniques, among them transport [27, 28], magnetization [29, 30], *ac* susceptibility [31], calorimetry [32], neutron diffraction [33], and muon spin rotation [34].

Disorder, present to some degree in all samples due to material imperfections, weakens superconductivity locally, thereby providing energetically favorable positions for vortices. This preferential pinning at random sites disrupts the ordered lattice, leading to a glassy phase. The effects of disorder are lower at higher temperatures, since thermal fluctuations cause vortices to spend less time on pinning sites. Still, even weak disorder is believed to destroy the long-range correlations of the vortex lattice [35]. The perfect lattice is replaced by the Bragg glass phase, in which quasi-long-range order is retained and the structure factor exhibits Bragg peaks with power-law decay [36]. Experimentally, Bragg peaks were detected in diffraction experiments on clean samples [33], indicating that quasi-long-range order is indeed retained.

At lower temperatures, the effects of disorder are dominant. With increasing magnetic field, the elastic caging potential of the vortices decreases more strongly than the the pinning energy [25]. At some critical value of the magnetic field, it is energetically preferable for vortices to reconfigure in order to better accommodate the local pinning potential, rather than the vortex-vortex interaction potential, and dislocation loops proliferate. The quasi-long-range order of the low-field Bragg glass is replaced by an entangled vortex glass phase [37, 38]. The critical field for this transition is temperature dependent, with fluctuations effectively weakening the pinning potential. This results in inverse melt-

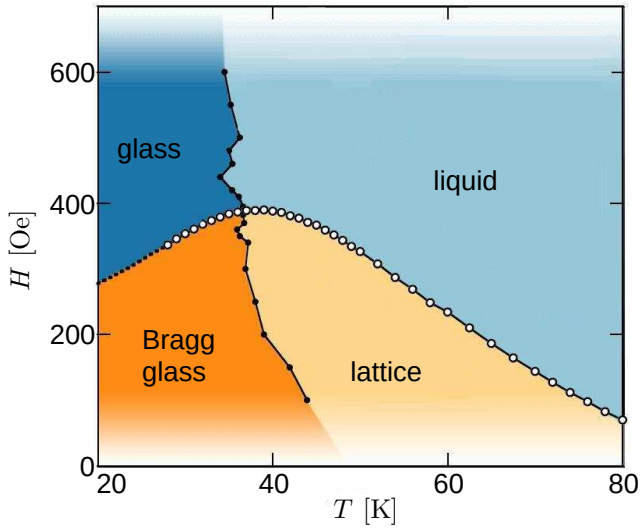

Fig. 3.3: *The thermodynamic phase diagram of BSCCO, measured experimentally, exhibits four distinct phases [40], separated by a first-order melting transition $H_m(T)$ (open circles) that is intersected by a second-order glass transition $H_g(T)$ (solid points).*

ing: a critical field that increases with increasing temperature. Experiments on BSCCO indicate that this inverse melting transition is first-order, and that it merges with the thermally-induced melting transition [39], thus forming a uniform first-order transition that separates the quasi-ordered Bragg glass from the various disordered phases.

This description of pristine high-T_c materials indicates that there are three relevant energy scales, whose interplay determines the various equilibrium phases of the $H-T$ phase diagram: elastic energy resulting from the repulsive vortex-vortex interactions, that tends to order the vortex lattice, pinning energy resulting from material defects, that leads to vortex displacement, and thermal fluctuations, that both weaken the pinning effects of material defects and dynamically displace the vortices from their lattice positions. The experimental phase diagram of pristine high-T_c materials is, as a result, complex. Figure 3.3 shows the $H-T$ phase diagram for the vortex matter in pristine BSCCO crystals. It is believed to consist of four separate phases, with boundaries defined by the melting and glass transitions $H_m(T)$ and $H_g(T)$. The $H_m(T)$ transition is understood to be a unified first-order melting transition. At elevated temperatures, this transition is thermally induced. At low temperatures, the $H_m(T)$ transition exhibits inverse melting from the

vortex glass phase to the quasi-long-range ordered Bragg glass phase as temperature is increased. The unified melting transition thus exhibits a cusp at intermediate temperatures. In BSCCO, an additional second-order transition $H_g(T)$ exists [40, 41]. Beneath the $H_m(T)$ transition, at $H_g(T)$, the vortex matter undergoes a second-order phase transition from the low-temperature Bragg glass to what is believed to be an ordered, thermally depinned vortex solid. Above the $H_m(T)$ transition, $H_g(T)$ denotes the transition from a low-temperature vortex glass phase, in which vortices are pinned, to a high-temperature liquid phase.

The thermodynamic phases of the vortex matter described above are obscured in experiments by many factors. Bulk pinning, perhaps the most problematic factor, leads to logarithmically slow relaxation of the vortex matter to its equilibrium state. At low temperatures, equilibrium behavior is inaccessible within realistic measurement times. The magnetic response of the sample therefore displays hysteretic behavior upon increasing and decreasing external field. This hysteresis closes at a temperature-dependent field, referred to as the irreversibility line, at which the thermal and elastic energies overcome the pinning potential. Additional factors that contribute to irreversibility are surface barriers [42] and sample geometry [43, 44]. Although the irreversibility line is dynamic in nature, whether or not it is the dynamic signature of an underlying thermodynamic transition is still an open question.

3.4.2 Samples With Correlated Disorder

Correlated disorder alters the high-T_c phase diagram. Such disorder is typically introduced using irradiation by heavy ions [46, 47], which create columnar defects (CDs) as they pass through the superconducting sample. These defects are random in the x-y plane perpendicular to the incident ion beam, but highly correlated along the z direction parallel to the beam axis. At high concentrations, when CDs outnumber vortices, the elastic energy of the vortices is negligible compared to the pinning energy. The system of vortices and CDs can be mapped onto the problem of Bosons on a two-dimensional random substrate [48]. The Bragg glass phase is replaced by the Bose glass phase, in

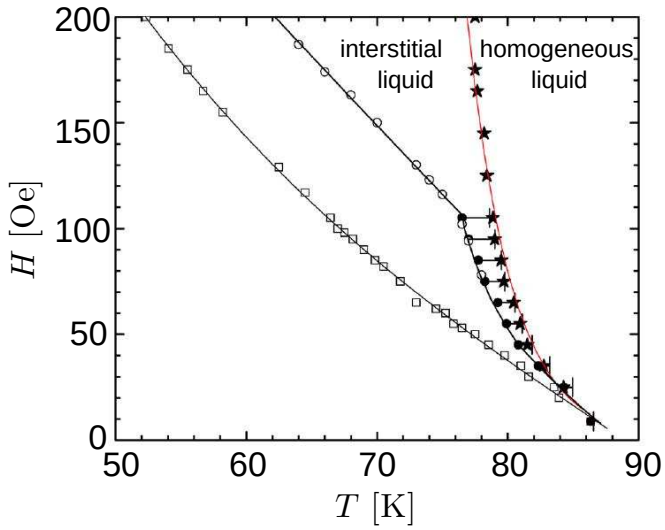

Fig. 3.4: *The thermodynamic phase diagram of a BSCCO sample with columnar defects, measured experimentally [45]. $B_\phi = 60$ G. The pristine melting line $H_m(T)$ (squares) is shifted in the presence of CDs to higher temperatures ($H_m^{\mathrm{CD}}(T)$, open circles). An additional delocalization transition at even higher temperatures $H_{dl}(T)$ (red line, stars), detected using transport measurements, separates the interstitial liquid from the homogenous liquid.*

which vortices are localized on columnar defects. When temperature is raised sufficiently, the Bose glass undergoes the so-called Bose-glass transition to a liquid phase, in which vortices are delocalized. The existence of an incompressible Mott insulator (MI) phase is also possible when the magnetic induction of the sample B exactly equals the matching field $B_\phi = \rho\phi_0$, where ρ is the density of the columnar defects. This model was extended [49] to include additional phases for $B > B_\phi$: a low-temperature weak Bose glass phase, in which both vortices residing at pins and those at interstitial sites are localized, an interstitial liquid phase at intermediate temperature, in which interstitial vortices are free to move but those at pinning sites are still pinned, and a homogenous liquid phase at higher temperature, in which all vortices are delocalized.

The experimental phase diagram of BSCCO irradiated by heavy ions with $B_\phi = 60$ G is shown in Fig. 3.4 [45]. Solid, interstitial liquid, and homogeneous phases are observed experimentally [50, 51, 45]. The melting transition from the solid phase to the interstitial liquid was observed to be a first-order transition for low fields. The equilibrium nature of the melting transition is complex, displaying at least one critical point at which the order

of the transition changes [52].

It is possible to introduce correlated disorder that is periodic in the x-y direction using various milling and lithography techniques, that create periodic holes in the superconducting material. These holes are typically limited in depth to a few microns. The varying diameter of these defects enables the pinning of multiple vortices to a single defect in some cases, leading to possible multi-quanta equilibrium states. The periodicity of the defects leads to additional possible phases of the vortex matter, particularly at matching fields, at which the vortex and defect densities are commensurate. Although these holes are an example of correlated disorder, the various Bose glass phases may be modified as a result of their x-y periodicity [53]. For periodic surface holes, even such a modified description is expected to be valid only within some finite depth from the surface of the superconductor.

Simulations of two-dimensional systems containing periodic pinning centers that allow only single-vortex occupancy demonstrate commensurate states at integer matching fields nB_ϕ, with permitted values of n depending on the geometry of the pinning centers [54]. Solutions of Ginzburg-Landau theory reveal additional commensurate states with multi-quanta vortices [55, 56] for more general sample and pinning center parameters. Different melting scenarios have been demonstrated for triangular and kagomé arrays at low matching fields [57], and for square pinning arrays both at and in-between matching fields [58]. The square pinning array at the first matching field displays three phases: a low-temperature pinned solid with square geometry, an unpinned ("floating") solid with triangular geometry, and a high-temperature liquid that lacks long-range order. At higher commensurate matching fields, the floating solid phase is not found, but an intermediate-temperature phase similar to the interstitial liquid is observed, in which some vortices are pinned to the centers, while interstitial vortices are mobile. Incommensurate fields close to matching display a pinned phase with extra vortices located at interstitial positions at low temperatures, a phase at intermediate temperatures in which some vortex motion is present with both interstitials and pinned vortices participating, and a phase at higher temperatures, in which all vortices are mobile. The temperature at which mobility is observed for incommensurate fields is lower than the melting tempera-

ture at the matching fields [58]. For the triangular and kagomé geometries, melting at the first matching field involves a low-temperature pinned solid and a high-temperature liquid only. Intermediate-temperature phases, in which some or all of the interstitial vortices are mobile, are observed at higher matching fields [57]. These melting transitions are expected to be most relevant to high-T_c superconductors [58].

There are few experimental data regarding the thermodynamic phases of high-T_c superconductors with periodic artificial pinning centers. Commensurate effects were observed in transport measurements on YBCO [59]. Multiple-quanta trapping by holes was observed for YBCO [60]. Thin crystalline BSCCO samples with fully-penetrating periodic holes exhibited integer [61] and rational [62] matching effects, in magneto-resistance and transport measurements, respectively. Similar samples with surface holes also displayed matching effects in magneto-resistance and critical current [63]. A single study using thick BSCCO samples with surface holes displayed integer matching in local magnetization [64]. The thermodynamic phases of high-T_c superconductors in the presence of periodic surface defects have not been studied extensively.

In Section 6.1 we present measurements of thick BSCCO crystals, partially patterned with periodic surface holes created by a focused ion beam. We use differential magneto-optics to explore how surface holes affect the compressibility of the vortex matter. We employ the shaking technique to investigate the equilibrium behavior of the vortex matter in the vicinity of the melting transition.

In Section 6.2 we present measurements of periodic magnetic patterns, measured with the Bragg magneto-optical microscope described in Section 5.2. This novel setup should provide a useful tool in future studies of the thermodynamic phases of the vortex matter in high-T_c superconductors.

4. Methodology

4.1 Differential Magneto-optical Technique

Magneto-optical measurements utilize a magneto-optical indicator (MOI) that is coated with a thin mirror on one side. The MOI is a material with large Faraday rotation that translates magnetic induction into rotation of the polarization of the light passing through it. The indicator is placed on top of the superconducting sample, with the mirror immediately above the sample. Incident polarized light passes through the indicator, is reflected off the mirror, and then passes through an analyzer with polarization axis at 90° to the polarization of the incident light. The 2D magnetic field distribution across the sample's surface is translated into an intensity image

$$I(x, y) = I_0 \sin^2 \Theta_{\mathrm{F}}(x, y)\,, \tag{4.1}$$

where I_0 is the intensity when the polarizer and analyzer axes are aligned, $\Theta_F(x, y) = 2dVB(x, y)$ is the Faraday rotation due to the local magnetic induction $B(x, y)$, d is the thickness of the indicator, and V is the Verdet's constant of the MOI. The MOIs used in the experiment were Bi-doped yttrium-indium-garnet films with typical thickness of $d \sim 5$ μm, grown on gallium gadolinium garnet, and coated with an aluminum layer approximately 0.1 μm thick. The Faraday rotation is wavelength-dependent, with a maximum near 500 nm. Typical Faraday rotation is 2° at an applied field of 100 Oe and a wavelength of 546 nm.

In differential magneto-optical (DMO) measurements, the difference between two magneto-optical images is calculated at each measurement point, with modulation of some experimental parameter between the first and second images. Typical modulation parameters are applied field H, temperature T, and current I. The modulation results in some

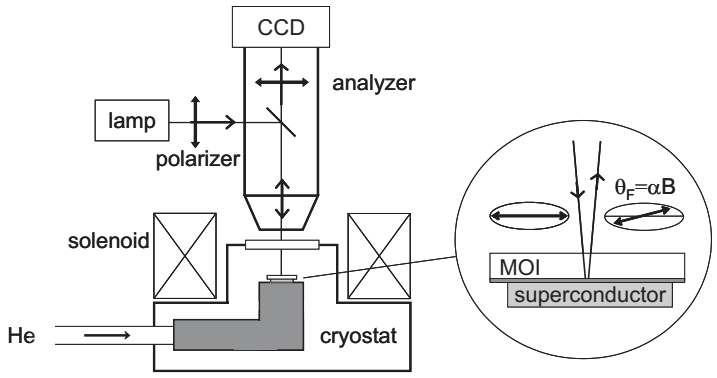

Fig. 4.1: *Schematic description of differential magneto-optical (DMO) setup.*

change in the distribution of the magnetic induction, from $B(x, y)$ to $B(x, y) + \Delta B(x, y)$. The intensity of the differential image can be approximated by

$$\Delta I(x, y) = 2I_0(2dV)^2(B\Delta B)\,. \tag{4.2}$$

4.2 Bragg Magneto-optical Technique

In the Bragg-MO system, we are interested in the first-order structure of the light reflected off the mirror at the bottom of the MOI. The incident light must therefore be coherent. The image of interest is the Fourier-space image. This means that the physical location that must be imaged is not the sample itself, but rather the location within the microscope that images Fourier-space - namely, the back focal plane of the microscope objective.

The MOI is placed as close as possible to the sample. Coherent polarized light is reflected off the mirror of the indicator. The magnetic flux quanta associated with vortices produce local, quasi-periodic maxima in the Faraday rotation of the reflected light. This leads to a diffraction pattern, which for a lattice with ideal periodicity follows Bragg's condition

$$\sin\theta_p - \sin\theta_i = p\lambda_{opt}/a_0\,, \tag{4.3}$$

where θ_i and θ_p are the incoming and outgoing angles of the light, respectively, λ_{opt} is the wavelength of the light, a_0 is the period of the lattice, and p is the diffraction order.

Calculations [65] show that the expected intensity ratio between the first and zeroth orders of the diffraction pattern, for a one-dimensional infinite square wave with amplitude ΔB, is

$$I/I_0 = \frac{4}{\pi^2}[\sin^2(dV\Delta B) - \sin^4(dV\Delta B)]\,, \tag{4.4}$$

where we have assumed that there is only polarization modulation (i.e., no phase or intensity modulation) as a result of the periodic magnetization. The change in polarization of the first diffraction order relative to the polarization of the zeroth order is [65]

$$\Delta\theta_{pol} = \pi/2 - dV\Delta B\,. \tag{4.5}$$

These two results imply that although the signal is on the order of $I/I_0 = 1.2 \times 10^{-4}$ for a modulation amplitude of 100 G [66], the signal to noise ratio can be improved greatly by using a polarizer that is aligned at 90° relative to the incoming (or zeroth order) polarization.

We now discuss the relation between the Fourier-space image of the vortex lattice within a superconducting sample and its degree of long-range order (LRO). Notations follow Ref. [67], though a similar description can be found in Ref. [68]. We note that in our case a MOI is placed above the sample. The MOI translates local magnetic induction into rotation of polarization. Therefore, in the following, the magnetic induction field should be replaced by a polarization modulation field.

The vortex lattice is described as a (two-dimensional) magnetic induction field $\rho(\mathbf{r})$. For an ordered phase, long-range periodicity allows the definition of a reciprocal lattice with reciprocal vectors $\{\mathbf{Q}\}$. The density field can be written as a Fourier-series

$$\rho(\mathbf{r}) = \rho_0 + \frac{1}{2}\sum_{\mathbf{Q}} \rho_{\mathbf{Q}}(\mathbf{r}) e^{i\mathbf{Q}\cdot\mathbf{r}}\,, \tag{4.6}$$

where ρ_0 is the mean induction.

The Fourier-space image depicts the static structure factor $S(\mathbf{q})$, given by

$$S(\mathbf{q}) = \sum_{\mathbf{Q}} \int_{\mathbf{r}} e^{i(\mathbf{q}-\mathbf{Q})\cdot\mathbf{r}} < \rho_{\mathbf{Q}}(\mathbf{r})\rho^*_{\mathbf{Q}}(\mathbf{0}) > \ . \tag{4.7}$$

The order-parameter correlator

$$C_{\mathbf{Q}}(\mathbf{r}) =< \rho_{\mathbf{Q}}(\mathbf{r})\rho^*_{\mathbf{Q}}(\mathbf{0}) > \tag{4.8}$$

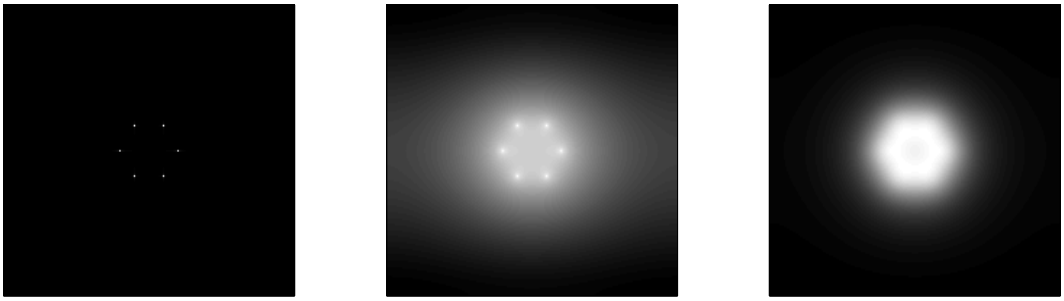

Fig. 4.2: *The three forms of $C_{\boldsymbol{Q}}(\boldsymbol{r})$ correspond to three Fourier-space images. From left to right: $C_{\boldsymbol{Q}}(\boldsymbol{r}) \rightarrow const$, $C_{\boldsymbol{Q}}(\boldsymbol{r}) \sim |\boldsymbol{r}|^{-\eta}$, and exponentially decaying $C_{\boldsymbol{Q}}(\boldsymbol{r})$ define long-range, quasi-long-range, and short-range translational order, respectively.*

determines the behavior of $S(\mathbf{q})$ in the following manner. If $C_{\mathbf{Q}}(\mathbf{r}) \rightarrow const$ for large $|\mathbf{r}|$, $S(\mathbf{q})$ has sharp Bragg peaks at $\mathbf{q} = \mathbf{Q}$. If $C_{\mathbf{Q}}(\mathbf{r}) \sim |\mathbf{r}|^{-\eta}$, the peaks broaden to power-law form. If $C_{\mathbf{Q}}$ decays exponentially for large $|\mathbf{r}|$, only diffuse peaks may exist. In these three cases, shown in Fig. 4.2, the lattice is said to posses long-range, quasi-long-range, and short-range translational order.

When considering a moving vortex lattice, there are three possible types of dynamic order: a disordered liquid, a moving (quasi-)crystal, and an additional state with (quasi-) LRO for only some subset of the original wave vectors $\{\mathbf{Q}\}$. The liquid displays short-range order and the (quasi-)crystal displays (quasi-)LRO. Since the additional dynamic state is a result of some applied driving force, it retains (quasi-)LRO either parallel or perpendicular to the direction of motion. This results in a layered, or smectic, structure. The Fourier-space image of such a state retains two Bragg peaks. The difference between the real and Fourier images of a moving (quasi-)crystal and those of a moving smectic are shown schematically in Fig. 4.3.

4.3 The Shaking Technique

Experimental investigation of the equilibrium properties of type II superconductors such as BSCCO can be performed only in the reversible region of the H-T phase diagram. This region is limited in pristine samples by the onset of irreversibility at lower temperatures due to pinning by defects. Irreversibility is enhanced in samples with artificial disor-

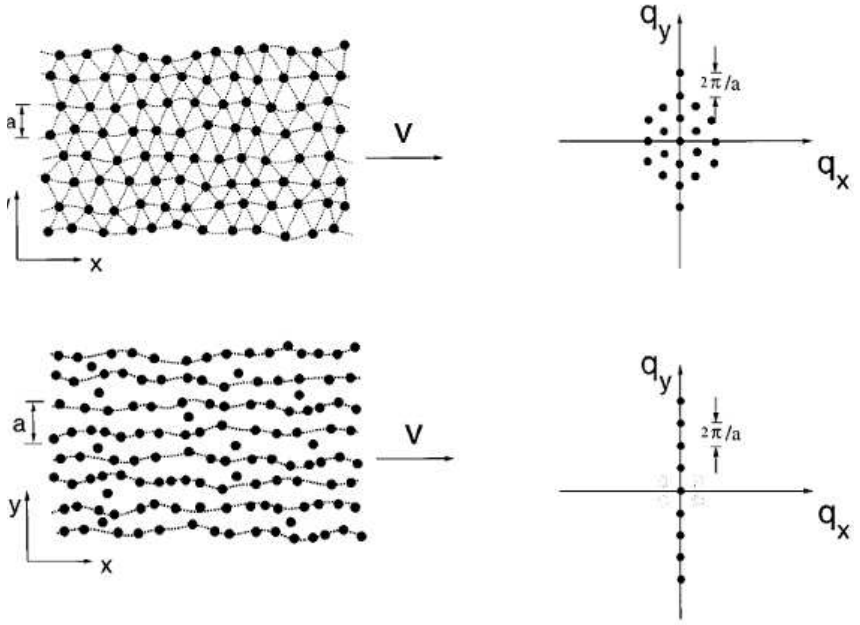

Fig. 4.3: *Schematic description of real-space (left) and Fourier (right) images of (a) (quasi-) crystal and (b) smectic states, taken from Ref. [67].*

der [69, 50]. The shaking technique reduces irreversibility using an oscillating magnetic field perpendicular to the applied *dc* field [70]. In BSCCO, the vortices can be regarded as a stack of pancake vortices in the individual layers, coupled by Josephson interactions. The in-plane shaking field penetrates the sample in the form of Josephson vortices that pass between the layers. A penetrating Josephson vortex locally deforms the stacked pancake structure through which it passes. This deformation is believed to enable depinning of pancake vortices that are trapped on point defects, thus enabling rapid relaxation of the pancake vortices to their equilibrium positions. The shaking method may also enable vortices to overcome surface [42] and geometrical [44, 71] barriers by breaking the vortices into segments. These segments could adjust independently to the energy barriers, thereby promoting relaxation. Shaking has been shown to reduce irreversibility in YBCO [70], pristine BSCCO [39, 40, 41], and in BSCCO samples with artificial defects [52], thus enabling the measurement of equilibrium properties of these materials in an extended region of the H-T phase diagram.

4.4 Fabrication of Periodic Surface Holes

To study the thermodynamic properties of samples with surface holes, we patterned limited regions of the surface of superconducting samples using a focused ion beam. This allowed comparison of pristine and patterned surface regions of the same samples. Holes were patterned on BSCCO samples using an FEI Strata 400 focused ion beam system (FIB). The samples were mounted either on sapphire, or on copper disks. Samples were electrically grounded to the FIB stubs during patterning to avoid surface charging. This was done using either silver epoxy, in which case the bottom of the sample was attached to gold contacts on the sapphire or to the copper disk, or with silver paint, in which case the paint extended from the stub to the surface of the sample. This paint was later removed, to allow optimal proximity between the sample and the MOI during measurements. The holes were patterned at FIB magnification of 650x (corresponding to a $\sim$ 195 μm-wide patterning region), and FIB current of 0.92 nA. Beam dwell time at each hole was 4.5 ms, and patterns were written in 140 passes.

Figures 4.4(a) and 4.4(b) show examples of hole profile and periodicity, respectively, imaged by SEM. Typical hole depth was approximately 1.4 μm. The lattice constant of the array in Fig.4.4(b) is 0.9 μm. Figure 4.4(c) shows a sample with patterned regions. The dimensions of each patterned region are approximately 170×170 μm^2.

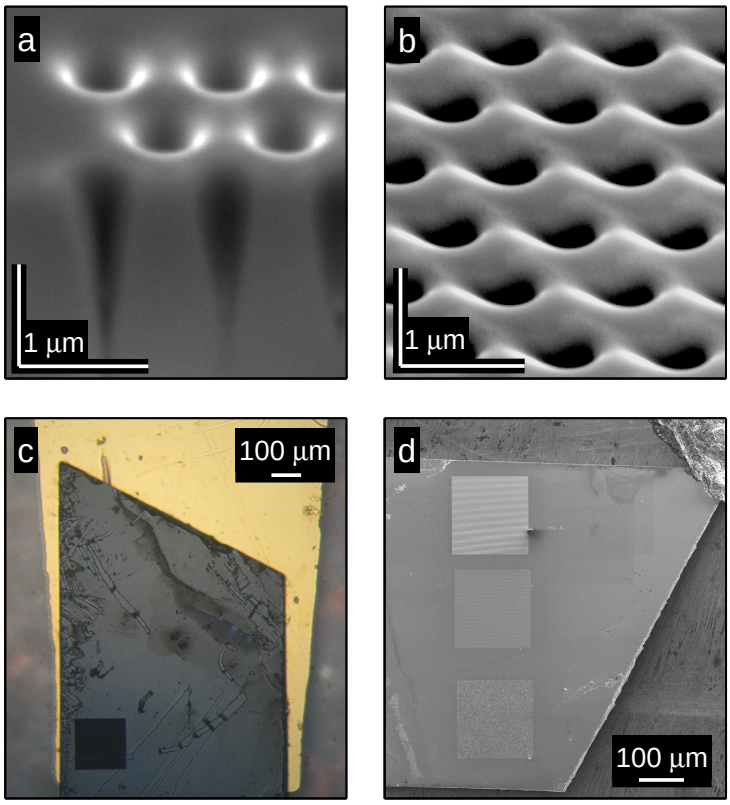

Fig. 4.4: *(a) A SEM image of the cross section of surface holes. Hole depth is* ~ 1.4 μm*. (b) Part of one of the arrays patterned by the FIB, imaged by SEM. The distance between holes is* 0.9 μm*, corresponding to a matching field of* $B_\phi = 29.5$ G*. (c) A BSCCO sample attached with silver epoxy to the gold contact, with a* 170×170 μm *patterned region (lower left corner). (d) A SEM image of a BSCCO sample with three* 170×170 μm *patterned regions. The sample is fixed to a copper disk by silver epoxy (top right corner).*

5. Experimental Setup

5.1 Differential Magneto-optical Setup

5.1.1 Cryogenics

Samples were measured in a continuous flow optical cryostat, with an extended cold finger. A heater and Lakeshore temperature sensor thermally coupled to the cold finger enabled control of the cold finger's temperature. An additional 50 Ohm heater and Lakeshore temperature sensor in the sample holder allowed fine tuning of the sample temperature, including temperature modulation with respect to the cold finger. Both heating loops were controlled using a Lakeshore 340 temperature controller. The sample holder incorporates a 44-pin chip carrier, thus enabling electrical contacts to the sample. The cryostat window is of fused silica, with AR coating.

Helium was supplied using a 110-liter storage vessel. Vessel pressure was kept constant at 4.5 psi using a backpressure regulator. Helium was transferred to the cryostat via a transfer line with a needle valve. Typical helium consumption was less than 1.3 liters of liquid helium per hour, allowing roughly 4 days of continuous measurement.

5.1.2 Microscope

Measurements were performed with a commercial Leica DMR microscope designed for polarized microscopy. Magnification was performed using 5x and 10x POL objectives, with additional optional magnification factors of $1, 1.25$, and 1.65 using lenses on the microscope body. The light source was a mercury lamp, which has a strong spectral line at 546 nm. Incoming light was filtered so that only green light entered. A hot mirror

blocked incoming UV and IR radiation.

5.1.3 CCD Camera

Images were measured by a Quantix 57 cooled CCD camera by Photometrics. The CCD size is 535 × 512 pixels, and pixel size is 13 × 13 μm^2. Images were digitized to 12-bit. Typical exposure times for single images were 0.2-0.6 sec.

5.1.4 X-Y-Z Magnet

The magnetic field was applied using an x-y-z water-cooled magnet, located outside of the cryostat and around the cold finger. The magnet consists of three Helmholtz coils, of which only the z and x were used in our experiments. The constants of the coils were 14.5 Oe/A (z) and 14.7 Oe/A (x). Two Kepco BOP 36-28MG power supplies supplied the current to the z and x coils. The coils were cooled by a Quantronix heat exchanger connected to the closed cooled-water circuit in the lab, allowing applied fields up to roughly 300 Oe in each coil without substantial heating. The current value of the z coil was supplied by two separate Yokogawa 7651 voltage sources for DC and modulation fields, to ensure an equal modulation amplitude at all DC fields. The current value of the x coil was supplied by an Agilent 8904A function generator. The applied current in the z-coil was measured on a 1 mOhm resistor using an HP 34401A.

5.1.5 Data Acquisition and Processing

A Labview program was used to control the measurement equipment, including the CCD camera. Acquired data was saved in 16-bit TIF format. All data analysis was performed using the Matlab 7.0.1 (R14) Image Processing Toolbox.

5.2 Bragg Magneto-optical Setup

5.2.1 Microscope

For reasons of practicality, we decided to build a combined standard magneto-optical and Bragg magneto-optical microscope. Below, we describe the details of both the standard-MO and the Bragg-MO optical paths.

5.2.1.1 Fourier-space Imaging

The optical path of the part of the setup that images Fourier space is shown in Fig. 5.1. For clarity, the optical elements are described in order of appearance along the optical path. The logic governing the choice of specific optical element parameters (such as focal length or lens size) is also described.

The light source for imaging of Fourier space must be coherent. We chose to work with a 532 nm laser, since the Faraday rotation per unit of magnetic induction of the MOIs peaks close to this wavelength. The laser beam enters the setup via an OzOptics single-mode, polarization-maintaining fiber, to ensure a purely Gaussian beam mode.

We now explain how the focal length $f_{g,in}$ of the focusing lens ($\mathrm{L_{g,in}}$) and its location are chosen. The diameter $d_{sample,g}$ of the beam incident on the sample is determined by the diameter D_{laser} of the original beam and the focal lengths of both the focusing lens ($\mathrm{L_{g,in}}$) and the objective (Obj), $f_{g,in}$ and f_{obj}, respectively, as

$$d_{sample,g} = D_{laser}\frac{f_{obj}}{f_{g,in}}\,. \tag{5.1}$$

The distance between the focusing lens and the objective is the sum of the focal lengths $f_{g,in} + f_{obj}$ so that the light incident on the sample will be plane-wave. The focusing lens for the incoming beam is a 1"-diameter plano-convex lens with anti-reflective (AR) coating for the visible range, with $f_{g,in} = 150$ mm, located 150 mm from the back focal plane of the objective. For $D_{laser} \sim 1.5$ mm and $f_{obj} = 20$ mm, we have an incident beam of $d_{sample,g} \sim 200$ μm on the sample.

Since the polarization of the beam is important, a minimum of optical elements is used between the entrance ($\mathrm{P_{g,in}}$) and exit ($\mathrm{P_{g,out}}$) polarizers. The entrance (exit) polarizer is

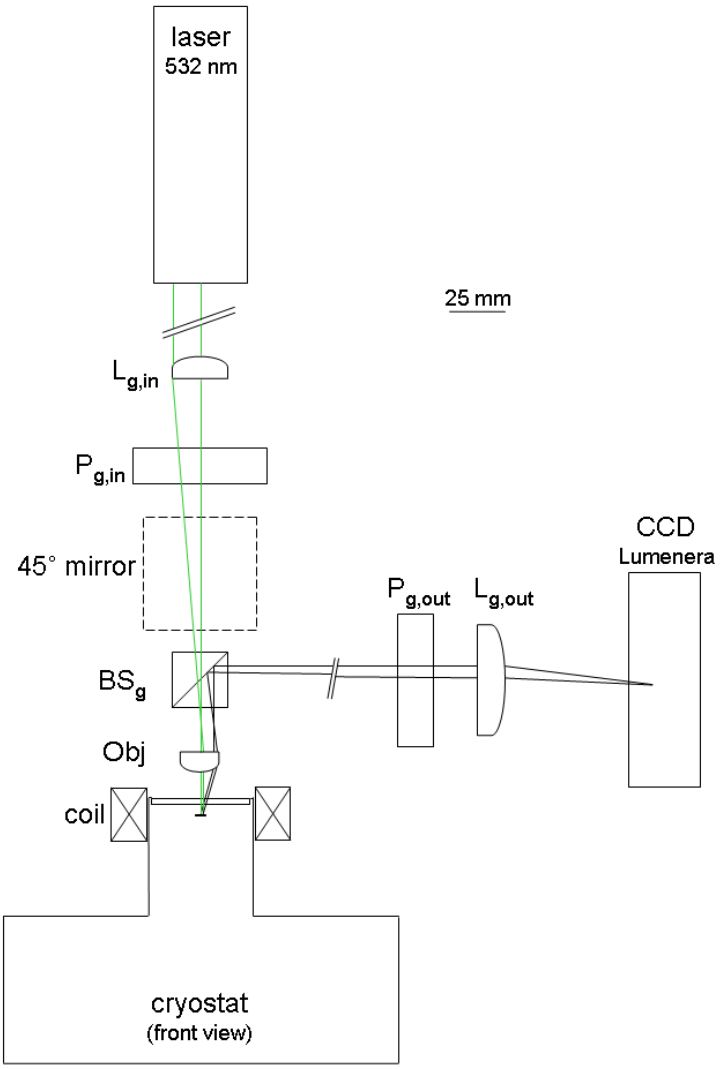

Fig. 5.1: *The Fourier-imaging part of the Bragg-MO setup. Incoming (green) and outgoing (black) rays of light drawn schematically to show where rays are parallel. The 45° mirror (dashed) is part of the real-space optical path, and can be translated to the side when imaging Fourier space.*

located immediately before (after) the beamsplitter (BS_g) on the path of the incoming (outgoing) light.

The beamsplitter (BS_g) should introduce minimal polarization distortion into the system. We chose a non-polarizing cube beamsplitter that leaves the relative phase of the two polarization components of the reflected beam unchanged.

The main parameter to consider when choosing the objective (Obj) is the angle θ of

the cone of light that it can collect. The numerical aperture (NA) of the objective, defined as NA $= \sin\theta$, sets the upper limit on the magnetic induction B_{max} and a lower limit on the lattice constant a_0 that can be imaged by the system, since

$$\lambda_{opt}\sqrt{\frac{\sqrt{3}B_{max}}{2\phi_0}} = \lambda_{opt}/a_{0_{min}} = \sin\theta_{p=1,max} = \mathrm{NA}\,. \tag{5.2}$$

We have assumed in the last equation that $\theta_i = 0$ and that the lattice is triangular. The objective currently in use is a Leica 10x POL objective with NA= 0.3, which corresponds to $\theta_{1,max} = 17.5°$, $B_{max} = 7.6$ G, and $a_{0_{min}} = 1.8$ μm.

The focal length of the imaging lens ($\mathrm{L_{g,out}}$) and its location determine the size and location of the image. The relations between the focal length $f_{g,out}$ of this lens, the distance of the lens from the back focal plane of the objective $u_{g,out}$ and the magnification of the diffraction pattern $M_{g,out}$ are given by

$$\begin{aligned} \mathrm{M} &= v_{g,out}/u_{g,out}\,, \\ \frac{1}{f_{g,out}} &= \frac{1}{u_{g,out}} + \frac{1}{v_{g,out}}\,. \end{aligned} \tag{5.3}$$

The required magnification for an image of dimension ≤ 10 mm (the diameter of the objective) on a ~ 6 mm CCD is $M \sim 0.6$. We chose an $f_{g,out} =$ 100mm lens with AR coating for the visible range. We set $u_{g,out} \simeq 250$ mm and $v_{g,out} \simeq 150$ mm, thus $M = 0.6$.

The diameter of the the imaging lens ($\mathrm{L_{g,out}}$) is chosen so that the diffraction pattern can be imaged entirely. The diameter of a single diffraction spot on the lens (neglecting effects due to the shapes of the beam and the sample) is

$$S_{spot} = 2h_{sample}u_{g,out}/f_{obj}\,, \tag{5.4}$$

where h_{sample} is the smaller of the diameter of the beam incident on the sample and the diameter of the sample. The distance of the spot from the center of the lens is

$$R_{spot} = f_{obj}\tan\theta_1\,. \tag{5.5}$$

For $h_{sample} = 200$ μm, $f_{obj} = 20$ mm, and $u_{g,out} = 250$ mm, the maximum diameter of the diffraction pattern on the imaging lens is $2R_{spot} + S_{spot} \simeq 18$ mm. The chosen lens ($\mathrm{L_{g,out}}$) for the outgoing beam is of 2" diameter. The camera for imaging Fourier space (CCD Lumenera) is located at a distance of $v_{g,out}$ from the imaging lens ($\mathrm{L_{g,out}}$).

5.2.1.2 Real-space Imaging

The optical path of the part of the setup that images real space is shown in Fig. 5.2. Optical elements are described in order of appearance along the optical path.

The light source (LED array) for imaging of real space is a 10×10 mm^2 LED array with a diffuser placed next to it on the optical path. We chose to work with a wavelength of 633 nm, since the Faraday rotation per unit of magnetic induction is still reasonably high at this wavelength. We chose not to work with green LEDs, as we are using a green laser for imaging Fourier space. This allows the option of imaging both Fourier and real space simultaneously at a later stage, using color filters immediately in front of the two imaging cameras. At this stage, we measure Fourier- and real- space sequentially, by moving a 45° mirror (see Figs. 5.1 and 5.2) in and out of the beamline. When in (out of) the beamline, real- (Fourier-) space is imaged.

The diffuser is a 5° diffuser that gives a more homogeneous light distribution than the original LED array without leading to major loss of intensity.

Two lenses ($L_{r,in,1}$ and $L_{r,in,2}$) collect and focus the incoming light before it passes through the objective. The first lens ($L_{r,in,1}$) has a relatively short focal length $f_{r,in,1}$ so that there will be little loss of intensity. This lens transforms the LED array into plane waves, and is located $f_{r,in,1}$ from the LED array. The second lens ($L_{r,in,2}$) focuses those plane waves to the back focal length of the objective (Obj), so that they will be incident upon the sample as plane waves. Its focal length is $f_{r,in,2}$ and it is located at a distance of $f_{r,in,2}$ from the back focal plane of the objective.

The polarization of the beam is important, though less critical than in the Fourier-imaging beamline. The entrance (exit) polarizer $P_{r,in}$ ($P_{r,out}$) is located immediately before (after) the beamsplitter (BS_r) on the path of the incoming (outgoing) light. Both incoming and outgoing beams are reflected off the removable mirror (45° mirror), placed at 45° with respect to both the red and green beamlines.

The sample acts as a multiple-point-source, and the light reflected off it is transformed into a plane wave by the objective (Obj). This light passes back through the Fourier-line beamsplitter (BS_g), is reflected from the real-space beamsplitter (BS_r), and is focused by

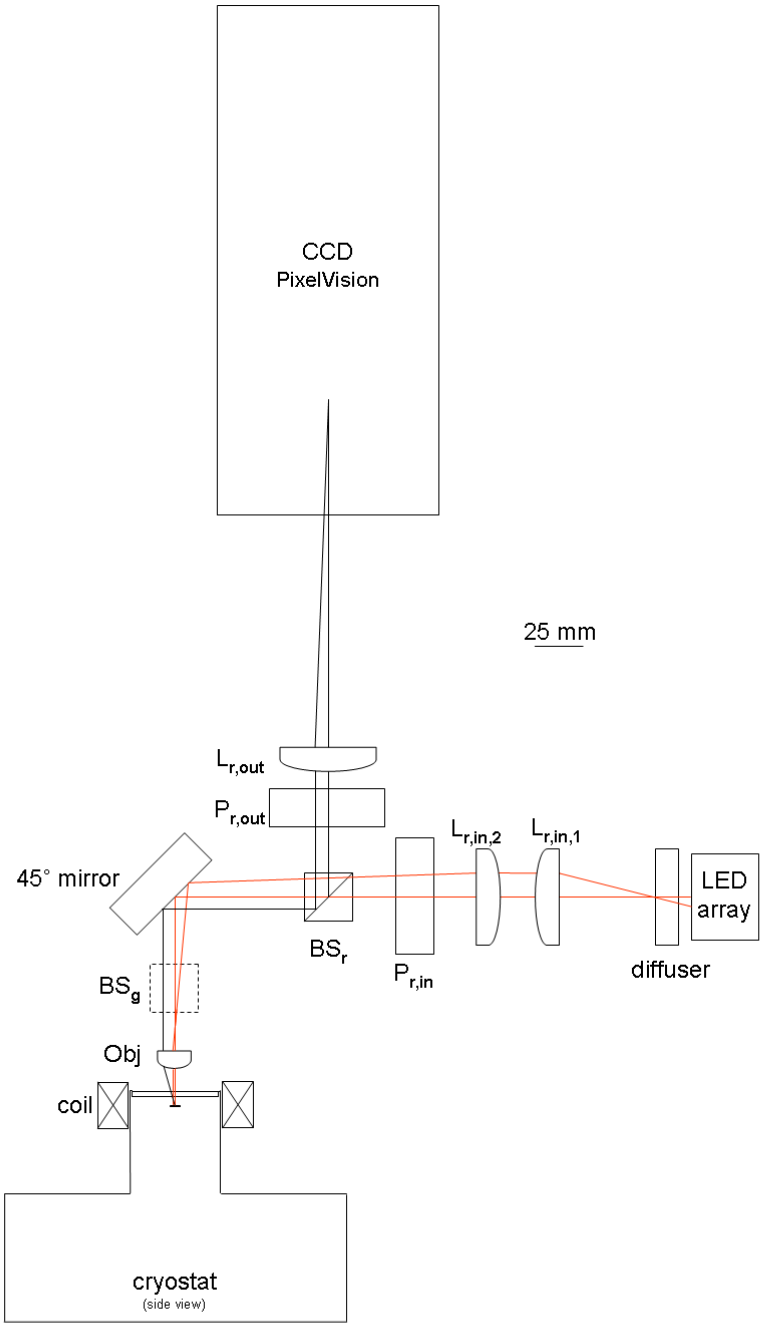

Fig. 5.2: *The real-space-imaging optical path. Incoming (red) and outgoing (black) rays of light drawn schematically to show where rays are parallel. The beamsplitter closer to the objective (dashed) is part of the Fourier optical path.*

a lens ($L_{r,out}$). This image is captured by a CCD (CCD PixelVision).

The focal length $f_{r,out}$ of the imaging lens $L_{r,out}$ determines the size of the image and

its location. The size of the image is given by

$$d_{r,image} = d_{sample} \frac{f_{r,out}}{f_{obj}} , \tag{5.6}$$

where d_{sample} is the diameter of the sample. The image is located on the focal plane of the lens, which coincides with the CCD chip. Using $f_{r,out} = 180$ mm and $f_{obj} = 20$ mm, with samples of size $d_{sample} \leq 1$ mm, we have $d_{r,image} \lesssim 9$ mm, which is compatible with our 12 mm CCD. The camera for imaging real space (CCD PixelVision) is located at a distance of $f_{r,out}$ from the imaging lens $\mathrm{L_{r,out}}$.

5.2.2 Cryogenics

The cryostat of the Bragg-MO setup is a Janis ST-500H continuous-flow optical cryostat. The diameter of the fused-silica cryostat window is 44.5 mm with a clear view of 36 mm and a thickness of 3 mm. The sample is located 4 mm beneath it, so that diffraction angles of $\theta \leq 68°$ are not blocked by the cryostat. The cryostat window is AR coated for the visible range. The cryostat reaches temperatures of 3.9 K and 4.7 K with and without pumping on the helium vent port, respectively.

Helium is supplied using a 110-liter storage vessel. Vessel pressure was kept constant at 4.5 psi using a backpressure regulator. Helium is transferred to the cryostat via a transfer line with a needle valve. Typical helium consumption was slightly under 1.3 liters of liquid helium per hour for cooling to 20 K or higher, and $\sim$ 3.5 liters per hour for cooling to below 5 K.

The temperature of the cold finger is measured and controlled using a Lakeshore 330 temperature controller with a Lakeshore temperature sensor and a 53 Ω heater, both located at the base of the cold finger. An additional Lakeshore temperature sensor is located on the sample holder directly beneath the sample.

The cold finger is wired with 12 twisted pairs that connect to the sample holder. These connections enable monitoring of sample temperature, and transport measurements.

5.2.3 Light Sources

The light source for the standard-MO optical path is a Norlux LED array. An Amrel power supply supplied the 0.4 mA (13 V) output to the LED.

The laser for the Bragg-MO optical path is a Suwtech DPGL-2100F CW laser with 100 mW output, powered by a Suwtech LDC-1500 adjustable power supply. The laser light is delivered via an Oz Optics single-mode, polarization-maintaining fiber with non-contact style fiber-couplers on both ends, all designed for a 532 nm wavelength. Typical laser intensities used were lower than 20 mW.

5.2.4 CCD Cameras

The Lumenera Infinity5 (CCD Lumenera) used for data acquisition is an interline camera with Peltier cooling. Its quantum efficiency is roughly 37% at 532 nm and its dark count is 0.5 $e^{-}p^{-1}s^{-1}$. The CCD size is 6.6×9 mm^2 with a resolution of 1040×1392.

The PixelVision Pluto14 (CCD PixelVision) camera used for imaging of real space is a frame-transfer CCD with a 12×12 mm^2 frame and a resolution of 1024×1024. Its quantum efficiency is less than 20%.

5.2.5 Magnet

An external magnetic field of up to 250 Oe can be applied using a 72 Oe/A coil that fits around the cold finger, outside of the cryostat. The sample is located at the center of the coil. A Toellner 8751 power supply supplies the current to the coils. The current value of the z coil was supplied by two separate Yokogawa 7651 voltage sources for DC and modulation fields, to ensure an equal modulation amplitude at all DC fields. The applied current in the coil was measured on a 1 mOhm resistor using an HP 34401A.

5.2.6 Data Acquisition and Processing

Varoius Labview programs were used to control the measurement equipment, including the CCD camera. The camera DLLs supplied by Lumenera were adapted to Labview

by Enrico Segre. All data analysis was performed using the Matlab 7.0.1 (R14) Image Processing Toolbox.

6. Results and Discussion

6.1 Vortex Matter in BSCCO with Periodic Surface Holes

In recent years, the effects of periodic holes on the dynamic and thermodynamic properties of superconducting materials have been studied extensively. Periodic holes have been introduced using various lithographic and milling techniques, yielding a wide range of hole dimensions and hole lattice geometries. The holes can be viewed as a form of correlated disorder along the c-axis of the material that is also periodic in the a-b plane.

Direct imaging experiments of low-T_c thin films with artificial periodic disorder have shown that highly ordered vortex states exist at integer nB_ϕ and fractional $(p/q)B_\phi$ matching fields, with n, q and p integers [72, 73]. Due to these ordered vortex states, such films have demonstrated commensurate effects in critical current [74, 75, 76, 77], magnetization [78], magneto-resistance [79, 80], and magnetic susceptibility measurements [81, 82, 83, 84]. Possible phases and phase transitions of the vortex matter have been inferred from these measurements. Enhanced flux creep rate for $B > B_\phi$ was thought to be evidence of a transition from an incompressible MI state to an interstitial liquid state [78]. Shapiro steps in transport measurements were understood to be a result of the coexistence of vortices pinned to artificial pinning sites and mobile interstitial vortices [85]. The behavior of the critical current was interpreted as evidence of two depinning energies, corresponding to the upper boundaries of the weak Bose glass and interstitial liquid phases [80]. Onsets of nonzero real and imaginary parts of the magnetic susceptibility were tentatively identified as the lower and upper phase boundaries of an interstitial liquid phase [83]. In addition to these states, the possibility of a saturation number $n_s > 1$, corresponding to n_s vortices at each pinning site, leads to multiple-quanta pinned vortex

states, which have been observed in many samples [76, 84].

There are fewer experimental data regarding the thermodynamic phases of high-T_c superconductors with periodic artificial pinning centers. The critical current in $YBa_2Cu_3O_7$ (YBCO) thin films exhibited integer commensurate effects [59] over a large temperature range. Scanning Hall probe measurements indicated that trapping of $\sim$ 15 flux quanta is possible for 2.5 μm-diameter holes close to T_c in YBCO [60]. Thin crystalline $Bi_2Sr_2CaCu_2O_{8+\delta}$ (BSCCO) samples with fully-penetrating periodic holes exhibited integer [61] and rational [62] matching effects, in magneto-resistance and transport measurements, respectively. Similar samples with surface holes also displayed matching effects in magneto-resistance and critical current [63]. A single study using thick BSCCO samples with surface holes displayed integer matching in local magnetization [64]. In these studies of BSCCO, the matching effects were visible in the field and temperature ranges at which the vortex matter is known to be in a liquid state in pristine crystals. No first-order melting step [30] was measured in these samples, and a full description of thermodynamic phases and transitions is lacking.

We studied the effect of periodic surface holes on the H-T phase diagram of BSCCO. Several samples were prepared and studied. Here we present a detailed investigation of a $2750 \times 740 \times 30$ μm^3 BSCCO crystal ($T_c \simeq 90.5$ K), with two triangular arrays of periodic holes patterned on the top surface using an FEI Strata 400 focused ion beam system. Figures 6.1(a) and 6.1(b) show SEM images of the hole profile and periodicity, respectively. The measured hole depth was approximately 1.4 μm. Hole diameter decreases from $\sim$ 0.6 μm at the sample surface to $\sim$ 0.3 μm at a depth of 0.7 μm. The lattice constant of both arrays was 0.9 μm, corresponding to a matching field of $B_\phi = 29.5$ G. The dimensions of each array were approximately 170×170 μm^2.

DMO measurements were performed by modulating the applied field $H||$c-axis by $\Delta H = 1$ Oe while sweeping temperature T at constant H or scanning H at constant T. Each measurement point required averaging over k CCD camera exposures, first at $H + \Delta H/2$ and then at $H - \Delta H/2$, and calculating a difference image. Each DMO image is the average of m such difference images. Using $k, m \sim 10$ with a typical exposure time of 0.3 sec yielded a typical modulation frequency of $\sim$ 0.33 Hz. Values of dB/dH

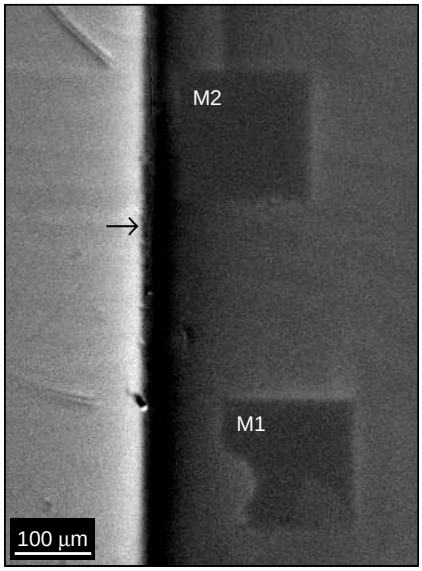

Fig. 6.1: *DMO image of part of a BSCCO sample. The edge of the sample is indicated by an arrow. Regions* M1 *and* M2*, of dimensions* 170×170 μm^2*, are patterned with* ~ 1.4 μm *deep surface holes, that form a triangular array with* $B_\phi = 29.5$ G.

were derived from the DMO images by dividing the local light intensity by the intensity of some region far from the sample, where it was assumed that $dB/dH = 1$ G/Oe. For quantitative data analysis, intensities were spatially averaged over typical area of $\sim 50 \times 50$ μm^2. Figure 6.1 shows a DMO image of part of the sample, taken at $T = 80$ K and $H = 21$ Oe. The average brightness of the patterned areas M1 and M2 is lower than that of the neighboring pristine sample. This is due to an elevated irreversibility line (IL) in the patterned areas as described below.

6.1.1 Enhanced Irreversibility

We first inspect the IL of the patterned regions. The IL is important in the context of possible Bose glass phases because it is thought to be the dynamic manifestation of the thermodynamic Bose glass transition [48]. In DMO measurements, reversibility of the vortex matter is quantified by modulating the applied field by ΔH, and measuring dB/dH, the change in the local magnetic induction due to the modulation. Strong pinning results in $dB/dH = 0$, whereas full reversibility corresponds to $dB/dH = 1$ G/Oe. The irre-

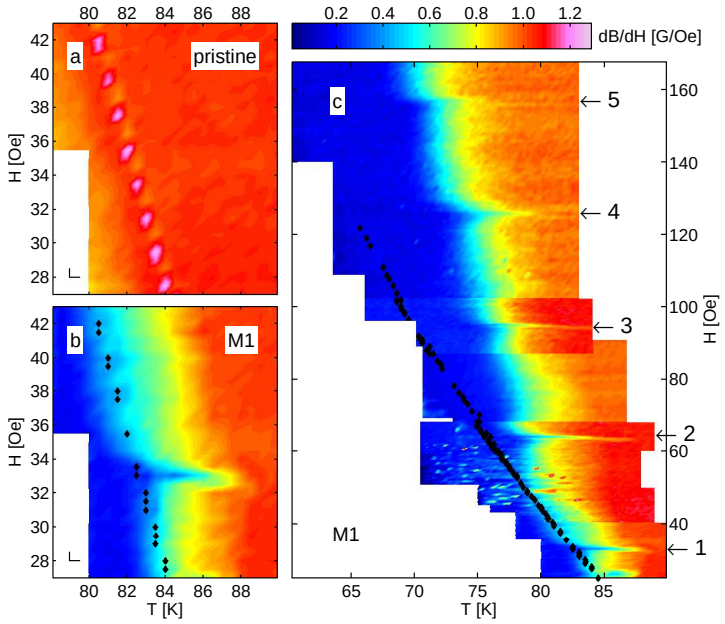

Fig. 6.2: *dB/dH, the change in magnetic induction due to an external field modulation of $\Delta H = 1$ Oe, for different sample regions, taken during T-scans. (a) A pristine region. The pristine melting line T_m appears as a series of paramagnetic peaks in dB/dH with values above 1 G/Oe (pink). This particular run was carried out on a sparse grid in T and H of 0.4 K and 0.5 Oe (denoted by the lines in the lower left corner). The apparent discontinuity in T_m is an artifact resulting from grid spacing being larger than the width of the melting peak. (b) dB/dH of region* M1 *in the vicinity of the first matching field, $B_\phi = 29.5$ G. dB/dH values are reduced compared to (a) and a narrow dip appears at $H = 33$ Oe. The location of the pristine melting line T_m is denoted by black points. (c) dB/dH in the patterned region* M1 *over a wide range of T and H. Matching effects (denoted by arrows) are visible at $H = 33, 64, 95, 126,$ and 157 Oe, consistent with integer multiples of the predicted $B_\phi = 29.5$ G. The pristine melting line T_m is denoted by black points. The patches in the data are a result of slightly differing setup parameters for the different experimental runs.*

versibility threshold in the following was chosen arbitrarily at $dB/dH = 0.8$ G/Oe, with T_{IL} (H_{IL}) denoting the temperature (external field) at which this threshold is reached. We emphasize that the resulting IL reflects the response of the vortex system at low frequencies. Transport measurements or DMO with current modulation could possibly map out additional boundary lines similar to the delocalization line of vortices from columnar defects [45], however, such measurements are beyond the scope of the present study. Figure 6.2 shows dB/dH for the pristine region (Fig. 6.2(a)) and patterned region M1

(Figs. 6.2(b) and 6.2(c)), measured by T scans at constant H.

Focusing on the pristine region (Fig. 6.2(a)), we see a series of sharp peaks in dB/dH with paramagnetic $dB/dH > 1$ (pink), corresponding to the first-order melting transition T_m from a low-temperature vortex solid to a high-temperature vortex liquid [86, 87]. The black dots in Fig. 6.2(b) show the pristine melting line T_m extracted from Fig. 6.2(a). The patterned region M1 (Fig. 6.2(b)), in comparison, shows no FOT. It does, however, exhibit two notable features. First, the IL of region M1 is shifted to higher temperature. This is seen by focusing on T_{IL} (yellow contour) in Figs. 6.2(a) and 6.2(b). T_{IL} of the patterned region M1 is significantly greater than T_{IL} of the pristine region, which occurs at temperatures lower than the pristine T_m. The second notable feature in Fig 6.2(b) is a narrow finger near $H = 33$ Oe, approximately 1 Oe wide, for $82 < T < 87$ K, in which dB/dH of M1 is suppressed.

Figure 6.2(c) shows dB/dH of patterned region M1 over a larger range of H and T. The pristine melting line T_m is plotted as black dots for comparison. The IL of M1 is clearly shifted to higher temperatures. Sharp fingers, or narrow regions of H in which dB/dH of M1 is highly suppressed, occur at $H = 33, 64, 95, 126$, and 157 Oe (denoted by arrows), consistent with integer multiples $B/B_\phi = 1, 2, 3, 4$, and 5 of the predicted matching field $B_\phi = 29.5$ G. The minima in dB/dH as a function of H at matching fields are of both dynamic and thermodynamic origin. Enhanced pinning at matching fields suppresses vortex motion, and hence also dB/dH. As discussed below, these minima also indicate narrow ranges of H with reduced equilibrium compressibility, since the compressional modulus c_{11} is proportional to dH/dB [88]. In addition to the fingers observed *at* integer B/B_ϕ, we see that T_{IL} *between* matching fields is step-like, with $T_{IL}(H)$ weakly dependent on H between matching fields, and shifts in $T_{IL}(H)$ occurring at matching fields. For example, $T_{IL} \approx 76.5$ K for $3 < H/B_\phi < 4$, and $T_{IL} \approx 74$ K for $4 < H/B_\phi < 5$ (yellow contour).

We now focus on the IL of the patterned regions below and in the vicinity of the first matching field. Figure 6.3 shows dB/dH measured simultaneously in the pristine region and in the patterned regions M1 and M2, for $B \lesssim B_\phi$. T_{IL} ($dB/dH = 0.8$ G/Oe, yellow contour) of the pristine region is located below the pristine melting line T_m. In region

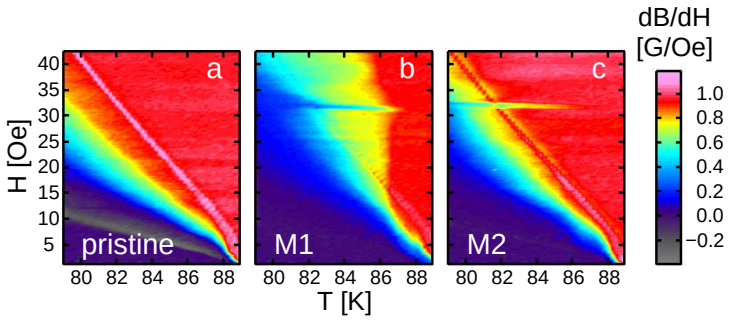

Fig. 6.3: *dB/dH for $B \lesssim B_\phi$, measured during T-scans. (a) dB/dH of a pristine region. The melting transition T_m appears as a line with $dB/dH > 1$ G/Oe (pink). The temperature T_{IL} at which the IL is located ($dB/dH = 0.8$ G/Oe, yellow) is found below T_m. (b) and (c) show dB/dH of patterned regions* M1 *and* M2*, respectively. T_{IL} of* M1 *is shifted to higher temperatures in comparison to the T_{IL} of the pristine region. This is observed also for* M2*, albeit less dramatically. There is an additional sharp shift upwards in T_{IL} of both* M1 *and* M2 *at $H = 33$ Oe, where $B = B_\phi$. Negative values of dB/dH (gray) correspond to negative permeability, due to geometrical barriers.*

M1 (Fig. 6.3(b)), T_{IL} is shifted to higher temperatures at all fields when compared to the T_{IL} of the pristine region (Fig. 6.3(a)). An additional sharp finger in the IL, extending to $T_{IL} \simeq 87$ K, occurs at $H = 33$ Oe, or $B = B_\phi$. The IL of patterned region M2 (Fig. 6.3(c)) is shifted somewhat less, yet it too displays a sharp shift to higher T at the matching field B_ϕ. The reason for the difference in the shift of the IL of the two arrays may be a result of the difference in the arrays' locations (M2 is closer to the sample's edge) or due to some difference in the holes of the two arrays, which are not identical and may have different pinning properties. Still, for both arrays the IL is shifted upward, with an additional sharp finger at B_ϕ. In BSCCO crystals irradiated with low concentration of CDs the sharp finger is absent. Instead, a kink is observed in the vicinity of B_ϕ which is believed to be the result of depinning of two different vortex populations. Below B_ϕ, T_{IL} is the temperature at which vortices located at CDs depin. Above B_ϕ, T_{IL} is the depinning temperature of interstitial vortices [45]. Also, fractional matching features have been observed [63] in BSCCO samples with periodic surface defects. We do not detect any fractional matching features in the IL of the patterned regions; the reason for this is not clear, but is consistent with results shown elsewhere [64].

6.1.2 Matching Features in the Presence of Shaking

The IL in BSCCO is known to be a dynamic feature of the phase diagram [89, 90, 39]. However, since it indicates a region of the phase diagram in which there is a change in the system's dynamic response, it may indicate an underlying thermodynamic transition that occurs at similar values of field and temperature. In order to detect a possible underlying FOT, and to determine whether the reduced dB/dH regions are truly a thermodynamic feature of the phase diagram, we studied the behavior of the first matching field in the presence of shaking. The shaking technique [70] utilizes an in-plane, ac magnetic field. It is known to suppress hysteretic behavior in BSCCO, enabling the observation of thermodynamic properties [39, 40, 41].

The effect of shaking is shown in Fig. 6.4, for the pristine and patterned regions M1 and M2 at 77 K. Increasing shaking amplitude $H_{ac}^{\perp}$ leads to a systematic increase in dB/dH, which saturates near 1 G/Oe, as expected for a fully penetrable sample. A feature common to all three plots in Fig. 6.4, and thus unrelated to the surface holes, is an abrupt change from zero to negative dB/dH at $\simeq 8$ Oe. Below $\simeq 8$ Oe, the sample is in the Meissner phase, with $B = 0$. $dB/dH < 0$ immediately above the Meissner phase corresponds to negative local permeability [91]. This effect, which occurs in BSCCO samples with platelet geometry, is a result of the geometrical barrier [43, 44] and the modulation of the vortex dome during the modulation cycle of the applied field $H \pm \Delta H/2$. This negative permeability is also visible as a gray strip at low fields in Fig. 6.3(a). It is interesting to note that the negative dB/dH values are not visible at the highest shaking amplitude, $H_{ac}^{\perp} = 121.8$ Oe. This indicates that the shaking field enables the vortices to overcome the geometrical barrier. Consequently, the local negative permeability changes to high positive local permeability, as seen in Figs. 6.4(a) and 6.4(c). This is the expected behavior in the absence of geometrical barriers, as demonstrated for prism-shaped samples [92].

There are two notable differences between the pristine (Fig. 6.4(a)) and patterned (Figs. 6.4(b) and 6.4(c)) regions. The first difference is the appearance of the matching feature in the form of a dip in dB/dH near 32 Oe, denoted by arrows in Fig. 6.4. Shaking extends the range of temperatures for which this dip is visible well into the vortex solid

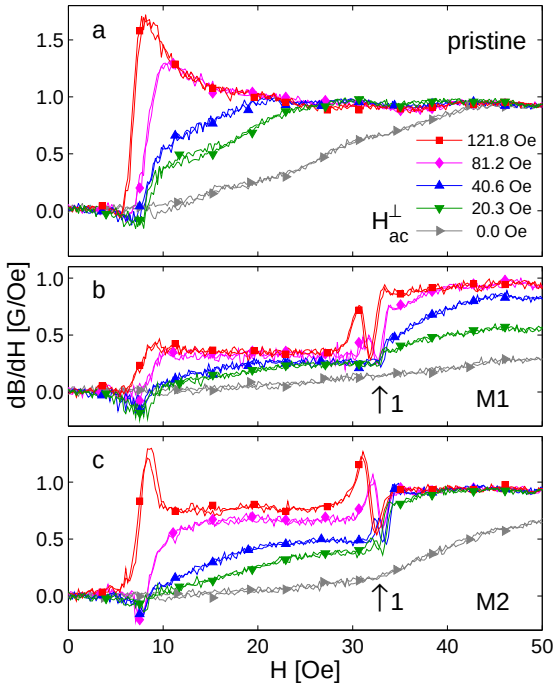

Fig. 6.4: *dB/dH vs. applied field H (scanned up and down) for different values of in-plane shaking amplitude $H_{ac}^{\perp}$, at $T = 77$ K for (a) the pristine region, (b) patterned region* M1*, and (c) patterned region* M2*. Arrows denote the first matching field. Data is shown for different values of applied $H_{ac}^{\perp}$ (from bottom to top): 0 (▷), 20.3 (▽), 40.6 (△), 81.2 (◇), and 121.8 (□) Oe. Shaking frequency was 15 Hz for all measurements. Symbols appear every 37 data points.*

region below T_m. Without shaking, the first matching feature is not visible at this temperature (77 K, see Fig. 6.2), due to the enhanced pinning in the vortex solid. With increased $H_{ac}^{\perp}$, the matching feature appears first as a step (Fig. 6.4(b), $H_{ac}^{\perp} = 20.3$ and 40.6 Oe) and then as a dip in dB/dH ($H_{ac}^{\perp} = 81.2$ Oe). In some cases, as shown in Fig. 6.4(c) for high $H_{ac}^{\perp}$, a peak appears in dB/dH immediately before the dip. The slight downward shift in H of the dip for increasing $H_{ac}^{\perp}$ probably results from the increased penetration of magnetic induction B at higher $H_{ac}^{\perp}$, resulting in the same $B = B_{\phi}$ at slightly lower values of applied field H. The dip in dB/dH corresponds to a reduction in the compressibility of the vortex matter at B_{ϕ}.

The second difference between the pristine and patterned regions in Fig. 6.4 can be seen away from the matching field. For the pristine region, the values of dB/dH increase gradually from $dB/dH \simeq 0$ at low field to $dB/dH = 1$ G/Oe at sufficiently

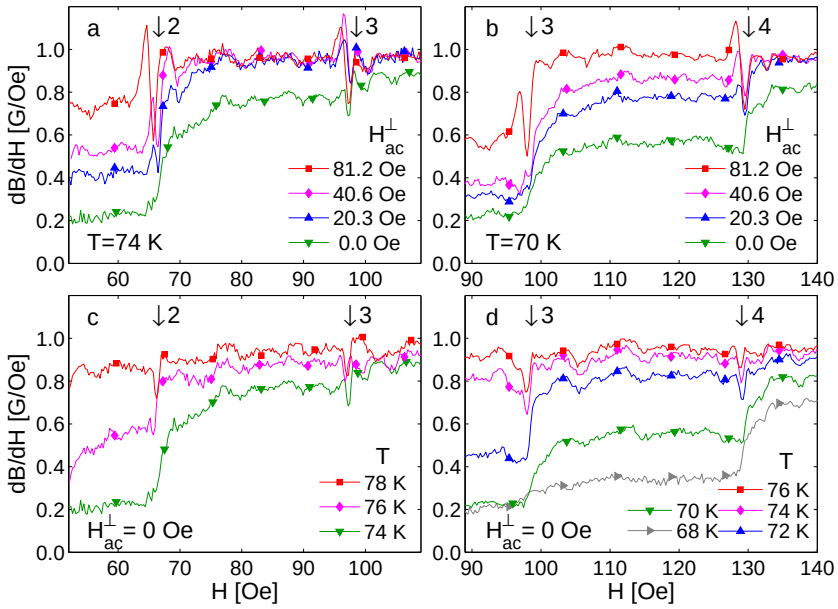

Fig. 6.5: *dB/dH of region* M2 *as a function of H for different temperatures T and shaking amplitudes $H_{ac}^{\perp}$. The effect of shaking is similar to the effect of temperature (see text). (a) Matching effects at $T = 74$ K, $B/B_\phi = 2, 3$, and (b) at $T = 70$ K, $B/B_\phi = 3, 4$. $H_{ac}^{\perp} = 0$ (∇), 20.3 ($\triangle$), 40.6 ($\diamondsuit$), and 81.2 ($\square$) Oe. (c) Matching effects at $T = 74$ ($\triangle$), 76 ($\diamondsuit$) and 78 ($\square$) K, $B/B_\phi = 2, 3$, without shaking. (d) Matching effects at $T = 68$ ($\triangleright$), 70 (∇), 72 ($\triangle$), 74 ($\diamondsuit$), and 76 ($\square$) K, $B/B_\phi = 3, 4$, without shaking. Arrows denote matching fields. Symbols appear every* 30 *data points.*

high applied field H. For the patterned regions, the behavior of dB/dH is plateau-like, with the matching feature dividing between neighboring plateaus. This can be seen in Fig. 6.4(b) for $H_{ac}^{\perp} = 81.2, 121.8$ Oe, and in Fig. 6.4(c) for $H_{ac}^{\perp} = 40.6$ Oe. These plateaus are consistent with the observed step-like behavior of T_{IL} during T-scans, as shown in Fig. 6.2(c). The plateaus in dB/dH appear between matching fields, where T_{IL} is almost independent of H. The step between the plateaus appears at $H = B_\phi$, consistent with the steps in T_{IL} that occur at $H = nB_\phi$. The value of dB/dH for each plateau in Figs. 6.4(b) and 6.4(c) increases with increasing $H_{ac}^{\perp}$. Figures 6.5(a) and 6.5(b) show the effects of shaking with different values of $H_{ac}^{\perp}$ for $B/B_\phi = 2, 3$ and $B/B_\phi = 3, 4$, respectively, for patterned region M2. The data for M1 are similar. Clearly the same matching features that appear for $B/B_\phi = 1$, namely a step in dB/dH for low $H_{ac}^{\perp}$ that develops into a dip for higher $H_{ac}^{\perp}$, are visible also for higher matching fields.

Interestingly, increasing T and increasing shaking amplitude $H_{ac}^{\perp}$ have similar effects on dB/dH immediately below the IL. This can be seen by comparing Figs. 6.5(a) and 6.5(c), in which dB/dH of region M2 in the vicinity of $B/B_{\phi} = 2, 3$ is plotted for different values of $H_{ac}^{\perp}$ and T, respectively. Increasing $H_{ac}^{\perp}$ and increasing T (bottom to top curves) both tend to increase dB/dH, and both have the effect of transforming the matching feature from a step to a dip. However, the overshoot in dB/dH immediately below the matching feature appears only at nonzero $H_{ac}^{\perp}$. Similar behavior is observed for $B/B_{\phi} = 3, 4$ in Figs. 6.5(b) and 6.5(d).

6.1.3 First-order Melting

We now address the question of first-order melting within the patterned regions in the presence of shaking. For the results shown below, we applied a 15 Hz, $H_{ac}^{\perp} = 81.2$ Oe shaking field. We find that shaking shifts the IL to lower fields and temperatures and thus enables the observation of a FOT in the patterned regions of the sample. Figure 6.6 shows detailed scans of the $H - T$ region in which the pristine T_m line intersects the $B/B_{\phi} = 1$ matching line. dB/dH is shown for both patterned regions and for the pristine region,

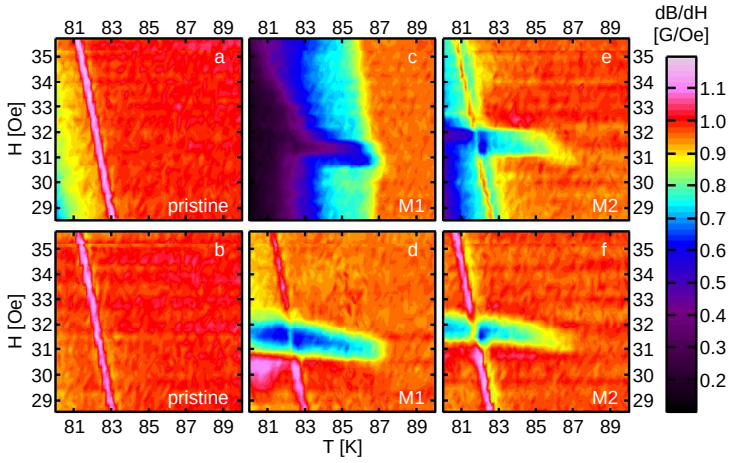

Fig. 6.6: *dB/dH as a function of H and T near the intersection of melting and $B/B_{\phi} = 1$ matching, without (top panels) and with (bottom panels) shaking. Shaking parameters were 15 Hz and 81.2 Oe. Results are shown for the pristine sample ((a),(b)) and patterned regions* M1 *and* M2 *((c),(d) and (e),(f), respectively).*

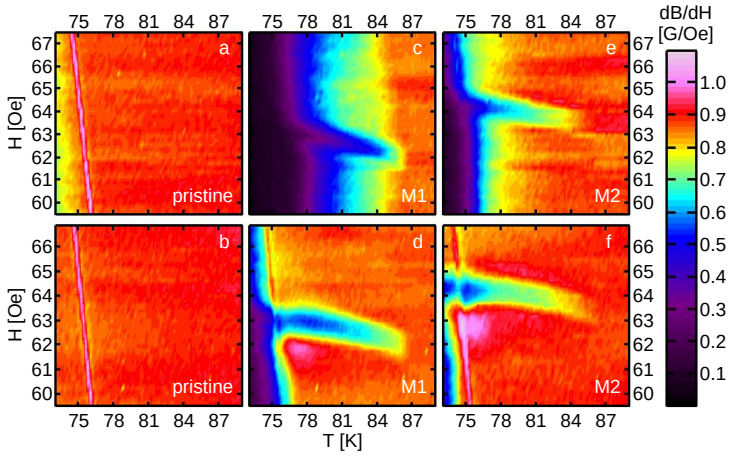

Fig. 6.7: *dB/dH as a function of H and T near the intersection of melting and $B/B_\phi = 2$ matching, without (top panels) and with (bottom panels) shaking. Shaking parameters were* 15 *Hz and* 81.2 *Oe. Results are shown for the pristine sample ((a),(b)) and patterned regions* M1 *and* M2 *((c),(d) and (e),(f), respectively). The slight curving of the matching effect to lower H for higher T in (c),(d),(e) and (f) is due to the increased penetration $B(H)$ at higher T.*

without and with shaking (top and bottom panels, respectively). For the pristine region (Figs. 6.6(a) and 6.6(b)), dB/dH at lower T and H is raised slightly by shaking, and the pristine melting line T_m, which appears as a line with paramagnetic $dB/dH > 1$ G/Oe (pink), remains essentially unchanged. For the patterned region M1, no FOT was visible without shaking (Fig. 6.6(c)). With shaking (Fig. 6.6(d)), a FOT became visible. It appears to be located at the same temperatures and fields as the pristine melting line T_m. Remarkably, the T_m line is clearly visible even at the bottom of the B_ϕ matching dip. For the patterned region M2, shaking was not needed to uncover the FOT (Fig. 6.6(e)). While shaking raised dB/dH values overall, it did not change the location or the nature of the FOT (Fig. 6.6(f)). Similar results are shown for $B/B_\phi = 2$ in Fig. 6.7. In this case, shaking was necessary to view the FOT in both patterned regions M1 (Fig. 6.7(c) and 6.7(d)) and M2 (Fig. 6.7(e) and 6.7(f)). Note that the location of the FOT of the patterned regions in the phase diagram is indistinguishable from the location of the pristine melting line, T_m. Moreover, T_m and the nB_ϕ lines seem to intersect with no apparent interaction, as if the periodic pinning potential of the holes has no effect on melting. No additional FOT was detected for either of the patterned regions. We emphasize that at the points

in the phase diagram where the FOT meets the matching fields, a contradictory behavior of the vortex lattice occurs. On one hand, at the FOT there is a *jump in vortex density*. On the other hand, at matching fields the vortex matter exhibits a *strongly enhanced compressibility modulus* $c_{11} \sim (dB/dH)^{-1}$ that exists both below and above T_m. This apparent contradiction is discussed below.

6.1.4 Discussion

In order to understand the observed behavior of the IL, we consider two possible physical scenarios [93]. In the first scenario, shown schematically in Fig. 6.8(a), we assume that each hole can pin only a single vortex. As a result, two vortex populations are present for $B > B_\phi$: vortices located at holes, and interstitial vortices located between holes. The interstitial vortices are subject to a caging potential caused by the vortices located at holes [53], that is assumed to be weaker than the pinning potential at holes, but stronger than the pristine pinning. This gives rise to a depinning transition of the interstitials, which we identify with T_{IL}, at a temperature above the pristine melting temperature T_m. Alternatively, we consider a scenario in which there is multi-quanta pinning by holes. We assume that below the IL, all vortices are located at holes, while above the IL, some vortices are depinned from holes, and thus mobile, as shown schematically in Fig. 6.8(b). Due to repulsion between pinned vortices, the pinning force per vortex is expected to decrease as a function of the number of vortices pinned to the hole [94]. We therefore assume that the pinned vortices residing at holes depin one at a time, as T is increased. Within this multi-quanta scenario, T_{IL} corresponds to the temperature at which the first vortices depin from holes. Either of the two scenarios must provide an explanation for the observed behavior of the IL: the plateaus in the IL *away from* matching, the shift in the IL to lower T and H in the presence of shaking, and the sharp dips *at* the matching fields.

We begin with the plateaus and steps in the IL. In the multi-quanta scenario, the maximum number of vortices per hole $n_{max}(T)$ is determined by temperature-dependent hole pinning strength and repulsive interactions between vortices located at the hole, and

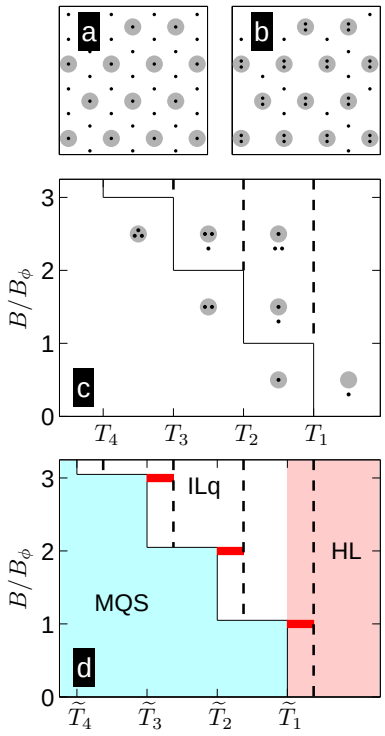

Fig. 6.8: *(a) and (b): A schematic view of the vortex matter for $B/B_\phi = 3$, within (a) the single-vortex pinning scenario, and (b) the multi-quanta scenario (see text). Grey circles indicate holes. Black dots indicate vortices. (a) In each unit cell of the pinning lattice, a single vortex is pinned to the hole and two vortices are interstitial. Below the IL, interstitials are pinned at interstitial positions. Above the IL, the interstitials are mobile. (b) In each unit cell, two vortices remain pinned to the hole. Below the IL, the third vortex is also pinned to the hole (not shown). Above the IL, it is depinned and mobile. (c) and (d): A schematic description of the steps in the IL, within the multi-quanta scenario, in the absence (c) and presence (d) of thermal fluctuations or shaking (see text). (c) The maximum number of quanta per hole $n_{max}(T)$ (solid black line) is expected to decrease as a function of T, resulting in temperatures T_n (dashed lines) above which holes pin $n-1$ vortices only, and additional vortices become mobile interstitials. Thus for each interval $(n-1) < B/B_\phi < n$, $T_{IL} = T_n$. (d) For $(n-1) < B/B_\phi < n$, thermal fluctuations shift T_{IL} (solid line) from T_n (dashed lines) to $\widetilde{T}_n < T_n$. At $B/B_\phi = n$, the vortex lattice remains stable to the temperature T_n due to a thermodynamic MI phase. Resulting phases include a multi-quanta-solid (MSQ, light blue) below T_{IL}, an interstitial liquid (ILq, white) above the IL that terminates at $\widetilde{T}_1$, a homogeneous liquid (HL, pink) above $\widetilde{T}_1$, and MI "fingers" at $B/B_\phi = n$ (red).*

decreases with increasing temperature [94]. We denote the temperature at which n_{max} decreases from n to $n-1$ by T_n (see dotted lines in Fig. 6.8(c)). We assume that for the applied fields $H \leq 6B_\phi$, all vortices are pinned to holes at sufficiently low T. As T is increased above T_n, holes may only pin $n-1$ vortices. Therefore vortices abruptly depin from holes occupied by n vortices, leaving $n-1$ vortices per hole. The depinned vortices are mobile, leading to a fast onset of reversibility. We therefore identify $T_{IL} = T_n$ for $(n-1) < B/B_\phi < n$. The resulting IL thus displays steps and plateaus, as shown schematically in Fig. 6.8(c). Finite temperature and slight hole variability are likely to cause some variation in $n_{max}(T)$ at different holes. This would lead to some smearing of the irreversibility transition and to a weak dependence of T_{IL} on B between matching fields due to different mixing of the T_n as field is varied. This schematic description neglects the effects of thermal fluctuations, which will be discussed later on. The IL shown in Fig. 6.2(c) (yellow contour) indicates that T_{IL} displays three discrete steps in the temperature range $T = 72 - 77$ K. The weak temperature dependence of the IL between matching fields, as well as the plateaus in dB/dH in Figs. 6.4 and 6.5, seem to indicate that the IL is not strongly affected by interactions between vortices at neighboring holes. Rather, it is governed by the hole pinning energy and the repulsion between vortices within a single hole, leading to the step-like T_{IL}. Within the single-vortex pinning scenario, in contrast, $T_{IL}(H)$ is the depinning temperature of interstitial vortices, that is expected to decrease rather smoothly with field as the density of interstitials increases.

We now address the the shift of the IL to lower temperatures in the presence of shaking. Shaking and increased thermal fluctuations seem to have a similar effect on the IL (see Fig. 6.5). Within the multi-quanta scenario both provide a mechanism for hopping of vortices between vacancies at holes, thus increasing the dynamic dB/dH and decreasing T_{IL}. Between matching fields and slightly below T_{IL}, the holes are below their full pinning capacity, so shaking may provide a way for vortices to hop between holes more easily, or to depin from holes and move to interstitial positions. The plateau-like behavior indicates that this shaking-induced hopping is roughly independent of the number of vacancies that exists. Instead, the degree of hopping or depinning is dependent on the balance between the roughly field-independent pinning energy of the n_{max}th vortex and the activation

energy of the applied shaking. Within the single-vortex pinning scenario, above the IL the interstitials are mobile, therefore immediately below the IL they are weakly pinned. Shaking will thus assist in overcoming the weak pinning potential, decreasing T_{IL}. The existence of the plateaus, however, cannot be easily explained in this case.

We now address the third experimental finding, namely the finger-like dips in dB/dH *at* matching fields. Focusing on Figs. 6.6 and 6.7, we see that unlike the rest of the IL, the temperatures at which the fingers terminate are *not* affected by in-plane shaking. This strongly suggests that unlike the IL, which is a *dynamic* feature of the phase diagram, the fingers at matching fields are a *thermodynamic* feature. A thermodynamic minimum with $dB/dH = 0$ would indicate a plateau in the equilibrium $B(H)$ and a diverging bulk modulus $c_{11} \sim \partial H/\partial B$ [88], clear signatures of the incompressible MI phase. The finite, positive minima observed in dB/dH (see Figs. 6.4(b), 6.4(c), and 6.5) correspond to a reduction in the positive slope of $B(H)$ at nB_ϕ. These finite values at nB_ϕ may be a consequence of the finite size of the patterned region, which prevents infinite divergence of c_{11}, or of the broadening of dB/dH due to the modulation of $\Delta H = 1$ Oe, which is at least as wide as the width of the dip. For samples with random defects, it has been argued that the MI phase is destroyed by repulsive vortex interactions, possibly retaining "lock-in" effects such as a finite peak in the bulk modulus c_{11} [95, 88]. In our measurements, however, the pinning is ordered. At matching fields, pinning energy and vortex-vortex interactions both stabilize the vortex lattice. In this case, observation of a MI phase is possible [95, 88]. We believe that the sharp matching features we observed in dB/dH at nB_ϕ, that are not affected by shaking, are a strong indication of thermodynamic MI phases.

The fingers of reduced dB/dH, or MI phases, may be understood in the context of the multi-quanta scenario. For $(n-1) < B/B_\phi < n$ and $T < T_n$, in the absence of thermal fluctuations, all vortices are pinned to holes (see Fig. 6.8(c)). The maximum number of vortices that can be pinned nB_ϕ/ϕ_0 is greater than the actual number of vortices B/ϕ_0, resulting in below-full occupancy, or "vacancies", at some of the multi-quanta holes. Thermal fluctuations (which were neglected in the schematic description in Fig. 6.8(c)) are expected to lead to vortex hopping between the vacancies, resulting

in enhanced vortex mobility. Thus, for $(n-1) < B/B_\phi < n$, vortex dynamics lead to a reduction in T_{IL} from T_n (Fig. 6.8(d), dashed lines) to some lower temperature $\widetilde{T}_n$. Exactly at matching, an additional thermodynamic consideration enters. The total hole capacity equals the number of vortices, and therefore there is a finite energy cost for adding an extra interstitial vortex. As a result, the equilibrium $B(H)$ will exhibit a plateau over a finite range of H, that is not affected by shaking. The corresponding minima in dB/dH, or equilibrium MI phases, may thus be observed up to T_n (red fingers in Fig. 6.8(d)).

The fingers of reduced dB/dH may also be partially understood within the single-vortex pinning scenario. At matching fields, we expect both the vortices at holes and the interstitials to be ordered in a configuration commensurate with the hole array, that enhances the pinning potential and may result in a thermodynamic MI phase. Although this picture is correct for commensurate matching fields ($B/B_\phi = 1, 3, 4, 7$, etc. for a triangular array of holes [54]), it is not strictly correct for incommensurate matching fields. At $B/B_\phi = 2$, for example, there are two interstitial positions with equal energy per unit cell. This would imply that hopping of interstitials is possible also *at* incommensurate matching fields, resulting in greater interstitial mobility, and hence a weaker matching effect. This is *not* what we observe in Fig. 6.2(c), where the fingers appear similar at the first and second matching fields.

We now consider the theoretical plausibility of the multi-quanta scenario. The condition given for multiple-quanta pinning in holes is [96] $r^3 > \xi\lambda^2$ for $\lambda \ll d$, where r is the hole radius, d is the inter-hole distance, and $\lambda = \lambda_0/\sqrt{1 - T/T_c}$ is the London penetration depth [89]. For $r = 0.2$ μm, and $\lambda_0 = 0.15$ μm [97], we may expect multiple-quanta vortices for $T \leq 88$ K for our sample.

We now estimate the number of vortices pinned at a hole as a function of temperature. We consider two physical possibilities, following Ref. [94]. The first is that the nth vortex is pinned as long as there is some force near the edge of the hole that pushes it inwards. This corresponds to a pinned state that may be metastable, depending on its free energy. The saturation number

$$n_s \approx r/(2\xi) \tag{6.1}$$

is the maximum n for which this occurs. The second possibility for multiple-quanta

pinning is to require an equilibrium pinned state, namely, the free energy of the nth vortex located in the hole must be lower than its free energy far from the hole. In this case, the number of pinned vortices is given by [94]

$$n_0 \approx \frac{1}{2} \ln \frac{r}{2\xi} / \ln \frac{2\lambda}{1.78r}. \tag{6.2}$$

Both n_s and n_0 decrease with T, which is consistent with the observed downward steps in $H_{IL}(T)$. Substituting $r = 0.2$ μm, $\xi_0 = 2$ nm, $\lambda_0 = 0.15$ μm, and $T_c = 90.5$ K, we obtain $n_s = 1 - 21$ for $T = 90.46$ K down to $T = 74.5$ K and $n_0 = 1 - 2$ for $T = 85.2$ K down to $T = 76.1$ K. Note that Eq. 6.2 was derived from the pinning energy of a *single* hole. In the case of an *array* of holes, one should compare the free energy of a pinned nth vortex to its free energy at the midpoint between two neighboring holes. At this midpoint, there are positive contributions to the free energy from the neighboring occupied holes. Thus a higher free energy of the pinned vortex, or $n > n_0$, would still be an equilibrium state of the system. Eq. 6.2 should therefore be considered a lower limit on the equilibrium number of vortices pinned to a hole. The fact that interactions should raise estimated occupation numbers was also noted by [56].

We now compare these theoretical estimates to the experimental values of n_{max}. We observed three decreasing steps in T_{IL} (see Fig. 6.2(c)), with $\widetilde{T}_6 \simeq 72$ K, $\widetilde{T}_5 \simeq 75$ K, and $\widetilde{T}_4 \simeq 77$ K. According to the schematic phase diagram plotted in Fig. 6.8(d), the values of $\widetilde{T}_n$ are lower than the temperatures T_n at which the n-th multi-quanta vortex depins in the absence of thermal fluctuations. From the schematic description in Fig. 6.8(c), we see that the difference $T_n - \widetilde{T}_n$ may be estimated from the difference in the T_{IL} at, and slightly away from, $B/B_\phi = n$. From Figs. 6.6(c) and 6.7(c), we estimate this difference to be $T_n - \widetilde{T}_n \sim 2$ K. T_6, T_5, and T_4 are thus 74, 77 and 79 K, respectively, or equivalently, $n_{max}(T < 74) = 6$, $n_{max}(74 < T < 77) = 5$, $n_{max}(77 < T < 79) = 4$, and $n_{max}(T > 79) = 3$. We find that the extracted n_{max} values are much lower than the estimated n_s, and slightly higher than the estimated n_0. Thus the equilibrium multi-quanta pinning scenario described by Eq. 6.2 is more plausible. Note, however, that Eqs. 6.1 and 6.2 are based on the assumption of fully penetrating holes; the number of vortices trapped by surface holes may be lower [98, 99].

Summarizing our discussion of the IL, the multi-quanta scenario provides a more consistent explanation as compared to single-vortex pinning, both for the steps in the IL and for the similar MI fingers at both commensurate and incommensurate matching fields. Indeed, recent simulations of BSCCO with surface holes similar to those in the experiment [100] indicate that multiple-quanta occupation of surface holes does occur, and that depinning may occur directly from holes.

Finally, we address the apparent contradiction of observing a FOT within the patterned regions *at matching fields* $B/B_\phi = 1, 2$, as shown in Figs. 6.6 and 6.7. The observed FOT occurs at the same field and temperature values as the pristine solid-liquid transition T_m, and we therefore assume that both transitions are of similar nature. This, however, seems to contradict the existence of MI phases at matching fields, since in the MI phase the vortex lattice is ordered, pinned, and incompressible, up to temperatures well above the pristine T_m.

The observed FOT can be understood qualitatively by taking the bulk beneath the surface holes into account. The surface holes are only $\sim$ 1.4 μm deep, whereas the sample is 30 μm thick. Although the depth at which vortices are still sensitive to surface patterning is not known exactly, magnetic decorations of BSCCO crystals with square Fe periodic surface patterns indicate that the hexagonal structure of the lattice is recovered fully just 4.5 μm beneath the pinning potential at low temperatures [101]. Thus one may expect that sufficiently deep below the upper surface, the vortex "tails" will undergo a first-order melting transition at the pristine T_m. At matching fields, however, the "tips" of the vortices at the surface are pinned to the periodic surface holes, and therefore behave as an incompressible solid. The resulting situation immediately above T_m is rather unique: the vortex "tips" are in a solid MI state, while the vortex "tails" are liquid. At the FOT, the vortex density in the bulk increases by $\Delta B/\phi_0$, where ΔB is the typical step in B at T_m. If the "tips" of the vortices were fully incompressible, this ΔB in the bulk would be completely shielded and unobservable at the top surface. Our data indicate, however, that within our experimental range of parameters the compressibility is high, but finite. Hence the MI top layer is sufficiently transparent to allow observation of the paramagnetic peak at the FOT of the underlying vortex "tails". We conclude that upon

increasing temperature, the FOT observed within the patterned region at matching fields indicates a transition from a solid bulk with an incompressible solid surface to a unique state of an essentially incompressible solid crust of vortex "tips" concealing a vortex liquid in the bulk.

No additional FOTs were observed, even in the presence of shaking. This indicates that the depinning line of the interstitial vortices, and the delocalization line of the vortices pinned to holes, are apparently *not* FOTs. More accurate magnetization measurements in the presence of shaking are needed to check for the existence of second-order thermodynamic transitions.

6.2 Bragg Magneto-optical Measurements of Periodic Magnetic Samples

The thermodynamic H-T phase diagram of the vortex matter in high-T_c superconductors displays a richness of phases and phase transitions [89]. Experimental study of the phase diagram relies on tools that are sensitive to physical properties of the vortex matter that vary from phase to phase. One of these properties is the degree of long-range order (LRO), which helps to differentiate between long-range-ordered solid, quasi-long-range-ordered Bragg glass, and disordered liquid and entangled glass phases. The degree of LRO in the vortex lattice is measured in diffraction experiments, which image the structure factor of the vortex lattice. Indeed, neutron diffraction measurements provided evidence for the Bragg glass phase in type II superconductors [102], and measured an abrupt decrease in the degree of LRO with increasing magnetic field at the melting transition in BSCCO [33].

The degree of LRO is also an important probe in dynamic measurements of the vortex matter. It has been predicted that the vortex lattice might change its geometry or orientation at a critical driving force, or driving current density [103]. A smectic phase has been predicted for the driven vortex lattice, in which the degree of LRO in the directions parallel and perpendicular to the current differs [67, 68]. The existing experimental evidence for the smectic phase is based on Bitter decoration [104], which is a problematic technique for dynamic measurements.

We built the unique Bragg-MO microscope with the ultimate goal of directly probing the structure of the vortex matter and its degree of LRO as a function of applied field and temperature, and applied driving current. Unlike neutron diffraction, the Bragg-MO microscope operates using laser light, utilizing a magneto-optical indicator (MOI) located directly above the sample. Periodic magnetic induction in the sample is translated by the MOI into a polarization grating, which results in a reflected diffraction pattern. By capturing the diffraction pattern of the magnetic induction due to the vortex lattice, the microscope aims to measure directly the orientation, geometry, and degree of LRO of the vortex lattice. Although the ultimate goal of this project, namely measurements of vortex matter, has not yet been reached, considerable progress has been made. We present

measurements of periodic magnetic recordings and describe MOI-sample proximity techniques. Finally, we discuss the direction of ongoing efforts.

6.2.1 Spatial and Magnetic Resolution

We created periodic magnetic patterns on commercial audiotape using sinusoidal patterns generated by a GW GFG-8020G function generator and a tape recorder with analog microphone input. Frequencies ranged from 0.1 to 10 KHz, corresponding to spatial

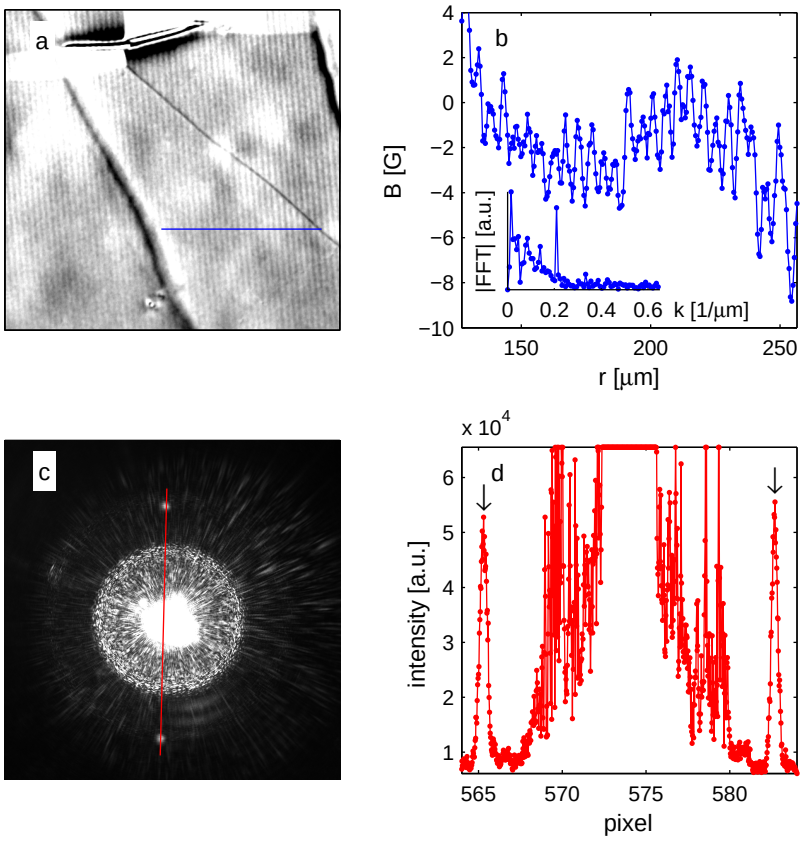

Fig. 6.9: *(a) Real-space image of* 10 *KHz magnetic recording, taken using the standard DMO setup. (b) Profile corresponding to the blue line in (a), calibrated according to Ref. [105]. Amplitude is less than* 4 *G. Inset: The Fourier transform of the profile (after subtracting its average) shows a peak at a spatial period of* 4.78 *µm. (c) Fourier-space image of recording shown in (a), taken using the Bragg-MO setup. (d) Profile corresponding to the red line in (c). Two first-order peaks are marked by arrows.*

frequencies of 470 to 4.7 μm. We were not able to record higher frequencies, due to limitations of the recording setup. We also had little control over the resulting amplitude of the periodic magnetic recording. Figures 6.9(a) and 6.9(c) show r- and k- space images of a 10 KHz recording measured at room temperature, taken using the standard DMO and Bragg-MO setups, respectively. The amplitude of the periodic magnetic induction shown in Fig. 6.9(a) was found to be ~ 4 G using the calibration method proposed in Ref. [105]. Figure 6.9(b) shows a profile taken from Fig. 6.9(a) (blue line) and its Fourier transform (see inset). The measured periodicity of the recording was $a_0 = 4.78$ μm. Figure 6.9(d) shows the profile taken from the Bragg-MO Fourier-space image in Fig. 6.9(c) (red line). The two first-order peaks of the diffraction signal are clearly observed.

The intensity of the zeroth order of the diffraction pattern provides information regarding the average magnetic induction of the region where the laser beam is incident. It can therefore be used as a probe of the average magnetic induction B_{avg} and of its derivative dB_{avg}/dH, when the external field is modulated. We measured the dependence of the intensity response ΔI of the zeroth order to varying modulation ΔH for different values

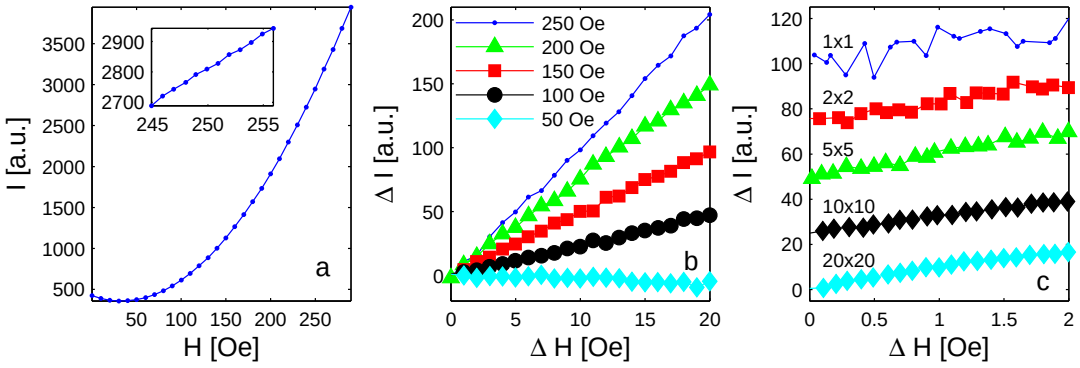

Fig. 6.10: *Measurements of intensity of zeroth order reflected off an MOI, taken at room temperature using* 30 *ms exposures. (a) Intensity of zeroth order I vs. applied field H. Inset: denser scan for vicinity of* 250 *Oe. (b) Intensity response ΔI to field modulation ΔH at applied fields of $H = 50, 100, 150, 200,$ and* 250 *Oe (bottom to top). (c) Intensity response ΔI to field modulation ΔH for applied field $H =$* 250 *Oe, for different averaging schemes:* 1x1, 2x2, 5x5, 10x10, *and* 20x20 *(top to bottom). Curves are offset by* 25 *for clarity. The indices pxq refer to averaging p times at both $H + \Delta H/2$ and $H - \Delta H/2$ before subtraction, and then averaging q times for data point.*

of applied field, at room temperature. The results for the dependence of I on applied field H (Fig. 6.10(a)) and of the response ΔI to the modulation ΔH (Fig. 6.10(b)) agree with the predicted Eqs. 4.1 and 4.2, for $B = H$. Fig. 6.10(b) demonstrates that the sensitivity of $\Delta I/\Delta H$ improves with increasing H, or equivalently, increasing offset with respect to crossed polarization. Fig. 6.10(c) shows that with sufficient averaging, the noise level of the differential measurement can be reduced to the target value of ≤ 0.1 G/Oe, which is the scale of both the step in the equilibrium magnetization at melting and the dip at matching fields in samples with periodic holes.

6.2.2 Proximity

The modulation in magnetic induction due to vortices in a superconducting sample is expected to decay exponentially as a function of height above the sample [66]. Proximity between the sample surface and the MOI is therefore of utmost importance. One way to measure the location-dependent air gap between the sample and the MOI is to count Newton rings, where each consecutive ring corresponds to an added height of $\lambda_{opt}/2$ above the sample [106], where λ_{opt} is the wavelength of the incident light. This technique has been employed successfully by other groups for imaging of single vortices [66, 107].

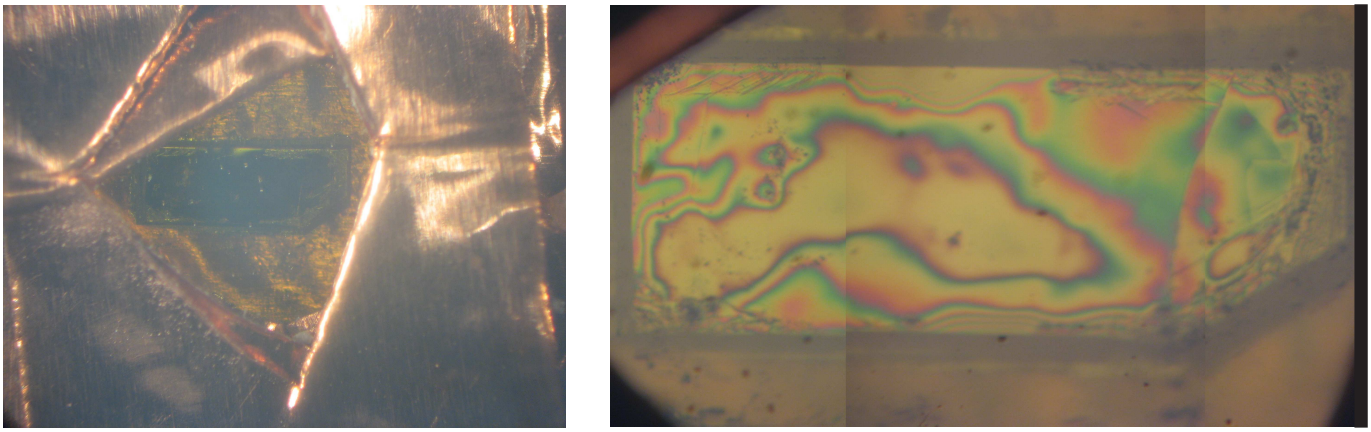

Fig. 6.11: *Left: MOI without mirror (yellow) taped to a* 2.8×1.1 mm^2 $NbSe_2$ *sample (dark gray) on sapphire substrate using copper tape. The trapezoid-shaped window was cut before taping. Right: Close-up on sample. Newton rings appear at height increments of* $\lambda_{opt}/2$*. The central region of this sample (enclosed by a single ring) is both flat and in excellent proximity to the MOI.*

Observation of Newton rings requires a MOI with no mirror and a flat, highly reflective sample. Removal of the aluminum mirror on the MOI is possible using a NaOH and H_2O solution (1:9 by weight). Flat samples are chosen using a ZYGO NewView 5032 surface analyzer. We have experimented with this technique and have succeeded in observing Newton rings in the following two ways. The first method, demonstrated in Fig. 6.11, is to tape the MOI to the sample using copper tape. A window is cut in the copper tape before taping so that the part of the MOI that is placed above the sample is not covered. Additional pieces of tape allow increased pressure to be applied in a semi-controlled way. The second method is to place three or four "pillars" of Apiezon N grease around the sample, so that they extend slightly above the sample surface. The MOI is then pressed gently onto the sample and the pillars. Slight adjustment is possible by applying pressure on the MOI. Both methods should demonstrate Newton rings at room temperature. From our experience, the pattern of the rings remains essentially the same as the sample and MOI are cooled, with typical changes of less than $\lambda_{opt}/2$. There is a possibility of sudden jumps in the pattern during cooling, indicating a shift in MOI placement, particularly when grease is used. So far, we have tested these methods with $NbSe_2$ due to its highly reflective surface. BSCCO samples will require a thin $(30 - 50$ nm) Al layer to improve reflectivity and to avoid heating of samples by the laser.

6.2.3 Discussion

There are two main factors that limit our ability to measure a diffraction pattern from the vortex lattice. First, MOI-sample proximity is not easily controlled. Second, the actual degree of LRO of the vortex matter in the superconducting sample is not known.

MOI-sample proximity can be improved using Newton rings to provide feedback, as discussed earlier. This method, however, is not easily applied. Recently, it has been suggested that the flux lines exiting the sample may be focused using a thin layer of superconducting Nb, evaporated on the back of the MOI or on the sample surface [108]. Nb is ideal as such a cap layer, due to its low penetration depth $\lambda \approx 40$ nm [109]. Single vortices within a thin Nb film sputtered on the back of a MOI were observed at

temperatures below ~ 9 K, the critical temperature of Nb [108]. Preparation of similar samples, evaporated directly onto the MOI, is an ongoing project.

The degree of LRO within the sample may be low, due to material impurities or to the behavior of the vortex matter at the values of external field and temperature to which we are currently limited. However, our results in Section 6.1 strongly indicate that periodic surface defects result in induced LRO. A superconducting sample deposited directly on the MOI, with periodic holes patterned on its bottom surface, should provide an ideal sample for the Bragg-MO setup.

7. Summary

The main goal of our measurements of high-T_c $Bi_2Sr_2CaCu_2O_{8+\delta}$ was to study the dynamic and the thermodynamic behavior of this material in the presence of periodic surface holes. These periodic holes were created on the surface of the samples using a focused ion beam. The samples were patterned in specific regions, to allow comparison of the patterned and pristine areas. The magnetic response of the samples to an external field was measured using differential magneto-optics with field modulation. We found that the dynamic irreversibility line of the patterned regions is shifted to higher fields and temperatures with respect to that of the pristine material. The irreversibility line displays step-like behavior, with weak temperature dependence between matching fields. These steps are consistent with a multi-quanta vortex scenario, in which vortices pinned at holes are depinned one by one as the temperature is increased. We also found that in narrow regions of the phase diagram corresponding to integer matching fields, the compressibility of the vortex matter is reduced considerably. In further measurements, magneto-optics combined with the shaking technique were used to investigate the equilibrium properties of the vortex matter in the vicinity of matching fields. These measurements indicated that the regions of reduced compressibility are equilibrium phases, namely Mott insulator phases of the vortex matter in the presence of periodic surface holes. Surprisingly, a first-order melting transition and its corresponding jump in vortex density occur even within these phases of reduced-compressibility. This apparent discrepancy is explained by the thickness of the samples with respect to the depth of the surface holes: the "tails" of the vortices located in the pristine bulk beneath the patterned regions undergo a first-order melting transition, which forces extra vortex "tips" through the surface, despite the reduced compressibility of the "tips".

The main goal of the construction of the Bragg magneto-optical microscope was to image the diffraction pattern of samples with periodic magnetic induction. The ultimate goal of such a microscope is to measure diffraction from the vortex matter within type II superconducting samples. From the diffraction pattern, it is possible to estimate not only the average density of the vortices, but also the degree of long-range order. This information would be invaluable in the study of the equilibrium and dynamic phases of the vortex matter. Using periodic magnetic recordings, we demonstrated that at room temperature, the Bragg-MO microscope is capable of measuring the diffraction pattern of samples with spatial periods as low as 4.8 μm, and spatial magnetic modulation amplitudes as low as 5 G. These limits were a result of our recording capabilities, and not due to intrinsic limitations of the microscope itself. From the intensity of the zeroth order of the diffraction pattern, and with sufficient averaging, we are able to detect a change in magnetic induction of less than 1 G in the region at which the laser beam is incident. Diffraction measurements from superconducting samples are the goal of ongoing research.

8. List of Publications

S. Goldberg, Y. Segev, Y. Myasoedov, I. Gutman, N. Avraham, M. Rappaport, E. Zeldov, T. Tamegai, C. W. Hicks, and K. A. Moler, Mott insulator phases and first-order melting in $Bi_2Sr_2CaCu_2O_{8+\delta}$ crystals with periodic surface holes, *Phys. Rev. B* **79**, 064523 (2009).

S. S. Banerjee, S. Goldberg, A. Soibel, Y. Myasoedov, M. Rappaport, E. Zeldov, F. de la Cruz, C. J. van der Beek, M. Konczykowski, T. Tamegai, and V.M. Vinokur, Vortex Nanoliquid in High-Temperature Superconductors, *Phys. Rev. Lett.* **93**, 097002 (2004).

This thesis summarizes my independent efforts.

The samples with surface defects were prepared with help from Yehonathan Segev and Yuri Myasoedov. Surface defects on test samples were patterned by Clifford Hicks from Stanford University.

Dan Oron was consulted when planning the Bragg-MO setup. Michael Golub calculated the relative intensities of the zeroth and first orders of the diffraction pattern from a one-dimensional periodic magnetic pattern. Beena Kalisky participated in construction and alignment of the Bragg-MO microscope, as well as in the measurements of diffraction from magnetic tapes.

References

[1] H. K. Onnes, Leiden Comm. **120b, 122b, 124c** (1911).

[2] W. Meissner and R. Ochsenfeld, Naturwissenschaften **21**, 787 (1933).

[3] J. G. Daunt and K. Mendelssohn, Proceedings of the Royal Society of London, Series A, Mathematical and Physical Sciences **185**, 225 (1946).

[4] W. S. Corak, B. B. Goodman, C. B. Satterthwaite, and A. Wexler, Phys. Rev. **96**, 1442 (1954).

[5] R. E. Glover and M. Tinkham, Phys. Rev. **104**, 844 (1956).

[6] A. A. Abrikosov and L. P. Gor'kov, Sov. Phys. JETP **12**, 1243 (1961).

[7] P. G. D. Gennes and G. Sarma, J. Appl. Phys. **34**, 1380 (1963).

[8] K. Maki, Prog. Theor. Phys. **29**, 333 (1963).

[9] S. Skalski, O. Betbeder-Matibet, and P. R. Weiss, Phys. Rev. **136**, A1500 (1964).

[10] M. A. Woolf and F. Reif, Phys. Rev. **137**, A557 (1965).

[11] J. L. Levine, Phys. Rev. **155**, 373 (1967).

[12] C. C. Tsuei and J. R. Kirtley, Rev. Mod. Phys. **72**, 969 (2000).

[13] F. London and H. London, Proceedings of the Royal Society of London, Series A, Mathematical and Physical Sciences **149**, 71 (1935).

[14] J. Bardeen, L. N. Cooper, and J. R. Schrieffer, Phys. Rev. **108**, 1175 (1957).

[15] V. L. Ginzburg and L. D. Landau, Zh. Eksp. Teor. Fiz. **20**, 1064 (1950).

[16] L. P. Gor'kov, Sov. Phys. JETP **9**, 1364 (1959).

[17] M. Tinkham, *Introduction to Superconductivity*, 2nd ed. (McGraw-Hill, 1996).

[18] A. A. Abrikosov, Sov. Phys. JETP **5**, 1174 (1957).

[19] U. Essman and H. Traüble, Physics Letters **24A**, 526 (1967).

[20] H. F. Hess, R. B. Robinson, R. C. Dynes, J. M. Valles, and J. V. Waszczak, Phys. Rev. Lett. **62**, 214 (1989).

[21] A. M. Chang *et al.*, Europhys. Lett. **20**, 645 (1992).

[22] K. Harada *et al.*, Nature **360**, 53 (1992).

[23] P. E. Goa, B. M. Hauglin, H., E. Ilyashenko, P. L. Gammel, and T. H. Johansen, Supercon. Sci. Technol. **14**, 729 (2001).

[24] J. G. Bednorz and K. A. Müller, Zeitschrift für Physik B Condensed Matter **64**, 189 (1986).

[25] V. Vinokur *et al.*, Physica C **295**, 209 (1998).

[26] D. R. Nelson, Phys. Rev. Lett. **60**, 1973 (1988).

[27] H. Safar *et al.*, Phys. Rev. Lett. **69**, 824 (1992).

[28] D. T. Fuchs *et al.*, Phys. Rev. B **54**, R796 (1996).

[29] H. Pastoriza, M. F. Goffman, A. Arribére, and F. de la Cruz, Phys. Rev. Lett. **72**, 2951 (1994).

[30] E. Zeldov *et al.*, Nature **375**, 373 (1995).

[31] R. A. Doyle, D. Liney, W. S. Seow, A. M. Campbell, and K. Kadowaki, Phys. Rev. Lett. **75**, 4520 (1995).

[32] A. Schilling *et al.*, Nature **382**, 791 (1996).

[33] R. Cubitt *et al.*, Nature **365**, 407 (1993).

[34] S. L. Lee *et al.*, Phys. Rev. Lett. **71**, 3862 (1993).

[35] A. I. Larkin and Y. N. Ovchinnikov, J. Low Temp. Phys. **34**, 409 (1979).

[36] T. Giamarchi and P. Le Doussal, Phys. Rev. B **52**, 1242 (1995).

[37] M. P. A. Fisher, Phys. Rev. Lett. **62**, 1415 (1989).

[38] D. S. Fisher, M. P. A. Fisher, and D. A. Huse, Phys. Rev. B **43**, 130 (1991).

[39] N. Avraham *et al.*, Nature **411**, 451 (2001).

[40] H. Beidenkopf *et al.*, Phys. Rev. Lett. **95** (2005).

[41] H. Beidenkopf *et al.*, Phys. Rev. Lett. **98** (2007).

[42] C. P. Bean and J. D. Livingston, Phys. Rev. Lett. **12**, 14 (1964).

[43] T. Schuster, M. V. Indenbom, H. Kuhn, E. H. Brandt, and M. Konczykowski, Phys. Rev. Lett. **73**, 1424 (1994).

[44] E. Zeldov *et al.*, Phys. Rev. Lett. **73**, 1428 (1994).

[45] S. S. Banerjee *et al.*, Phys. Rev. Lett. **93**, 097002 (2004).

[46] L. Civale *et al.*, Phys. Rev. Lett. **67**, 648 (1991).

[47] M. Konczykowski *et al.*, Phys. Rev. B **44**, 7167 (1991).

[48] D. R. Nelson and V. M. Vinokur, Phys. Rev. B **48**, 13060.

[49] L. Radzihovsky, Phys. Rev. Lett. **74**, 4923 (1995).

[50] S. S. Banerjee *et al.*, Phys. Rev. Lett. **90**, 087004 (2003).

[51] M. Menghini *et al.*, Phys. Rev. Lett. **90**, 147001 (2003).

[52] T. Verdene *et al.*, Phys. Rev. Lett. **101**, 157003 (2008).

[53] I. B. Khalfin and B. Y. Shapiro, Physica C **207**, 359 (1993).

[54] C. Reichhardt, C. J. Olson, and F. Nori, Phys. Rev. B **57**, 7937 (1998).

[55] M. M. Doria and S. C. B. de Andrade, Phys. Rev. B **60**, 13164 (1999).

[56] G. R. Berdiyorov, M. V. Milošević, and F. M. Peeters, Phys. Rev. B **74** (2006).

[57] M. F. Laguna, C. A. Balseiro, D. Domínguez, and F. Nori, Phys. Rev. B **64**, 104505 (2001).

[58] C. Reichhardt, C. J. Olson, R. T. Scalettar, and G. T. Zimányi, Phys. Rev. B **64**, 144509 (2001).

[59] A. Castellanos, R. Wördenweber, G. Ockenfuss, A. v.d. Hart, and K. Keck, Appl. Phys. Lett. **71**, 962 (1997).

[60] A. Crisan *et al.*, Phys. Rev. B **71** (2005).

[61] S. Ooi, T. Mochiku, S. Ishii, S. Yu, and K. Hirata, Physica C **445–448**, 260 (2006).

[62] S. Ooi, T. Mochiku, M. Gaifullin, and K. Hirata, Physica C **460–462**, 1220 (2007).

[63] S. Ooi, T. Mochiku, and K. Hirata, Physica C **463–465**, 271 (2007).

[64] S. Ooi, T. Mochiku, S. Yu, E. Sadki, and K. Hirata, Physica C **426–431**, 113 (2005).

[65] M. Golub, private comm.

[66] P. E. Goa, H. Hauglin, A. A. F. Olsen, M. Baziljevich, and T. H. Johansen, Rev. Sci. Instrum. **74**, 141 (2003).

[67] L. Balents, M. C. Marchetti, and L. Radzihovsky, Phys. Rev. B **57**, 7705 (1998).

[68] P. Le Doussal and T. Giamarchi, Phys. Rev. B **57**, 11356 (1998).

[69] B. Khaykovich *et al.*, Phys. Rev. B **57**, R14088 (1998).

[70] M. Willemin *et al.*, Phys. Rev. Lett. **81**, 4236 (1998).

[71] M. V. Indenbom and E. H. Brandt, Phys. Rev. Lett. **73**, 1731 (1994).

[72] K. Harada *et al.*, Science **274**, 1167 (1996).

[73] S. B. Field *et al.*, Phys. Rev. Lett. **88**, 067003 (2002).

[74] A. T. Fiory, A. F. Hebard, and S. Somekh, Appl. Phys. Lett. **32**, 73 (1978).

[75] A. N. Lykov, Solid State Commun. **86**, 531 (1993).

[76] D. J. Morgan and J. B. Ketterson, Phys. Rev. Lett. **80**, 3614 (1998).

[77] V. V. Moshchalkov *et al.*, Phys. Rev. B **57**, 3615 (1998).

[78] M. Baert, V. V. Metlushko, R. Jonckheere, V. V. Moshchalkov, and Y. Bruynseraede, Phys. Rev. Lett. **74**, 3269 (1995).

[79] J. I. Martín, M. Vélez, J. Nogués, and I. K. Schuller, Phys. Rev. Lett. **79**, 1929 (1997).

[80] E. Rosseel *et al.*, Phys. Rev. B **53**, R2983 (1996).

[81] V. V. Metlushko *et al.*, Europhys. Lett. **41**, 333 (1998).

[82] V. Metlushko *et al.*, Phys. Rev. B **59**, 603 (1999).

[83] L. E. De Long *et al.*, Physica C **369**, 118 (2002).

[84] A. V. Silhanek, S. Raedts, M. J. Van Bael, and V. V. Moshchalkov, Phys. Rev. B **70**, 054515 (2004).

[85] L. Van Look *et al.*, Phys. Rev. B **60**, R6998 (1999).

[86] N. Morozov, E. Zeldov, D. Majer, and M. Konczykowski, Phys. Rev. B **54**, R3784 (1996).

[87] A. Soibel *et al.*, Nature **406**, 282 (2000).

[88] C. Wengel and U. C. Täuber, Phys. Rev. B **58**, 6565.

[89] G. Blatter, M. V. Feigel'man, V. B. Geshkenbein, A. I. Larkin, and V. M. Vinokur, Rev. Mod. Phys. **66**, 1125 (1994).

[90] D. Majer, E. Zeldov, and M. Konczykowski, Phys. Rev. Lett. **75**, 1166 (1995).

[91] N. Morozov, E. Zeldov, D. Majer, and B. Khaykovich, Phys. Rev. Lett. **76**, 138 (1996).

[92] N. Morozov, E. Zeldov, M. Konczykowski, and R. A. Doyle, Physica C **291**, 113 (1997).

[93] O. M. Stoll, M. I. Montero, J. Guimpel, J. J. Åkerman, and I. K. Schuller, Phys. Rev. B **65**, 104518 (2002).

[94] G. S. Mkrtchyan and V. V. Schmidt, Sov. Phys. JETP **34**, 195 (1972).

[95] C. Wengel and U. C. Täuber, Phys. Rev. Lett. **78**, 4845 (1997).

[96] A. I. Buzdin, Phys. Rev. B **47**, 11416 (1993).

[97] T. Jacobs, S. Sridhar, Q. Li, G. D. Gu, and N. Koshizuka, Phys. Rev. Lett. **75**, 4516 (1995).

[98] A. Bezryadin, Y. N. Ovchinnikov, and B. Pannetier, Phys. Rev. B **53**, 8553 (1996).

[99] S. Raedts, A. V. Silhanek, M. J. Van Bael, and V. V. Moshchalkov, Phys. Rev. B **70**, 024509 (2004).

[100] Y. Y. Goldschmidt and M. Opferman, unpublished.

[101] Y. Fasano, M. Menghini, and F. de la Cruz, Physica C **408–410**, 474 (2004).

[102] T. Klein *et al.*, Nature **413**, 404 (2001).

[103] D. Li, A. M. Malkin, and B. Rosenstein, Phys. Rev. B **70**, 214529 (2004).

[104] F. Pardo, F. de la Cruz, P. L. Gammel, E. Bucher, and D. J. Bishop, Nature **396**.

[105] R. J. Wijngaarden *et al.*, Rev. Sci. Instrum. **72**, 2661 (2001).

[106] F. A. Jenkins and H. E. White, *Fundamentals of Optics*, 4th ed. (McGraw-Hill, 1976).

[107] M. Terao, Y. Tokunaga, M. Tokunaga, and T. Tamegai, Physica C **426-431**, 94 (2005).

[108] M. Tokunaga, T. Tamegai, and T. H. Johansen, Physica C **437-438**, 331 (2006).

[109] B. W. Maxfield and W. L. McLean, Phys. Rev. **139**, A1515 (1965).

תקציר

בעבודה זו מדדנו דגמים של מוליך-על בעל T_c גבוה $Bi_2Sr_2CaCu_2O_{8+\delta}$ (BSCCO) עם חורים מחזוריים בפני השטח שנוצרו על-ידי אלומת יונים מכוונת באמצעות מגנטו-אופטיקה דיפרנציאלית עם מודולציית שדה. מצאנו שקו האירברסיביליות הדינמי של האזורים בעלי החורים מוזז לערכי שדה מגנטי ולערכי טמפרטורה גבוהים מאלו של האזורים ללא החורים. בקו האירברסיביליות ישנן מדרגות עם תלות חלשה בטמפרטורה בין שדות ההתאמה, בהן צפיפות המערבולות היא כפולה שלמה של צפיפות החורים. אנו מסבירים כיצד מדרגות אלו תומכות בנוכחות מערבולות בעלי יותר מקוונט אחד של שטף מגנטי. אנו מוצאים שבאזורים צרים של דיאגרמת הפאזה הH-T המתאימים לשדות ההתאמה הדחיסות של החומר המערבולתי מצומצמת משמעותית. מדידות בסביבה של שדות ההתאמה באמצעות מגנטו-אופטיקה בשילוב עם שיטת הניעור הראו כי אזורים אלו בעלי דחיסות מצומצמת הינם מצבי מבודד Mott תרמודינמיים של החומר המערבולתי בנוכחות החורים בפני השטח. באופן מפתיע, מעבר פאזה מסדר ראשון מתרחש גם בתוך אותם האזורים בעלי הדחיסות המצומצמת. אנו דנים בסתירה לכאורה זו.

בפרויקט קשור, בנינו מיקרוסקופ Bragg מגנטו-אופטי חדשני שמדמה את תבנית ההתאבכות של דגמים בעלי תבנית אינדוקציה מגנטית מחזורית. הדגמנו שמיקרוסקופ זה מסוגל למדוד התאבכות מהקלטות מגנטיות מחזוריות עם מחזור מרחבי ומשרעת שמתקרבים לאלו של שריג המערבולות בתוך מוליך-על מסוג שני. בנוסף הדגמנו שסדר האפס של תבנית ההתאבכות מהווה כלי למדידת האינדוקציה המגנטית הממוצעת. הראנו שעם מספיק מיצוע, סדר האפס מסוגל למדוד אות מסדר גודל של 0.1 G, שזהו סדר הגודל הן של המדרגה במגנטיזציה במעבר-הפאזה מסדר ראשון בBSCCO והן של הירידות הלוקאליות בתגובה המגנטית בשדות ההתאמה בדגמי BSCCO בעלי חורים מחזורים בפני השטח.